Computer simulation of the effect of deformation on the morphology and flow properties of porous media

Sahar Bakhshian and Muhammad Sahimi

Phys. Rev. E **94**, 042903 — Published 24 October 2016

DOI: 10.1103/PhysRevE.94.042903

Computer Simulation of Effect of Deformation on the Morphology and Flow Properties of Porous Media

Sahar Bakhshian and Muhammad Sahimi[†]

Mork Family Department of Chemical Engineering and Materials Science, University of Southern California, Los Angeles, California 90089-1211, USA

We report on the results of extensive computer simulation of the effect of deformation on the morphology of a porous medium and its fluid flow properties. The porous medium is represented by packings of spherical particles. Both random and regular, as well as dense and nondense packings are used. A quasi-static model based on Hertz's contact theory is used to model the mechanical deformation of the packings, while the evolution of the permeability with the deformation is computed by the lattice-Boltzmann approach. The evolution of the pore-size and pore-length distributions, the porosity, particles' contacts, the permeability, and the distribution of the stresses that the fluid exerts in the pore space are all studied in detail. The distribution of the pores' lengths, the porosity, and the particles' connectivity change strongly with the application of an external strain to the porous media, whereas the pore-size distribution is not affected as strongly. The permeability of the porous media strongly reduces even when the applied strain is small. When the permeabilities and porosities of the random packings are normalized with respect to their pre-deformation values, they all collapse onto a single curve, independent of the particle-size distribution. The porosity reduces as a power law with the external strain. The fluid stresses in the pore space follow roughly a log-normal distribution, both before and after deformation.

PACS number(s): 81.05.Rm, 47.56.+r, 47.11.-j, 91.60.Np, 83.10.-y

[†]E-mail: moe@usc.edu

I. INTRODUCTION

An important class of porous materials includes those that are deformed by, for example, a large external pressure or shear, or by absorbing liquids that cause swelling. Important examples of such porous materials include consolidating clays [1], biopolymers, cell membranes, food stuff, and hydrogels [2,3], snow [4,5], paper [6,7], diapers [8,9], cakes of particles that are formed on the external surface of a filter [10], aggregates that are formed by flocculation [11], articular cartilage, a soft biomaterial swollen by water [12], foams [13-16], materials for drug delivery [17], and soil and rock at large depths where the pressure is large [1,18-20]. An important practical example of current interest is sequestration of carbon dioxide in geological formations. When CO_2 is injected into a porous formation and enters the pore space, together with the brine in the pore space it causes deformation in the structure of the solid matrix through its interaction with the pores' walls and the saline water that already exists in the pores.

Over the past two decades, several theoretical studies of deformable porous media have been undertaken. Such studies may be divided into three major classes. In one class are macroscopic theories that are based on volume [21] or ensemble averaging [22] of the continuum equations of transport. One writes down the conservation laws at the microscale, supplements them with constitutive relations that are empirical or semi-empirical, and then averages the equations at the macroscale in order to derive the governing equations at that scale.

Mixture theories constitute the second class of models of deformable porous media. They are based on the macroscale conservation laws, coupled with the second law of thermodynamics and entropy inequality. But, as pointed out by Hassanizadeh and Gray [23-25], since entropy inequality is not included in averaging at the microscale to arrive at the macroscale equations, one cannot obtain relationships that link macroscopic thermodynamic variables. In addition, such mixture theories do not utilize any information at the microscale.

The third class of models of deformable porous media represents a combination of the first two, which we refer to as the hybrid mixture theories (HMTs) [23-25]. Originally developed by Hassanizadeh and Gray [23,24], the HMTs begin with the microscopic conservation laws, average them to derive the macroscopic equations, and then invoke the entropy inequality in order to derive the constitutive equations, such as the generalized Darcy's law for slow flow of fluids through a macroscopic deformable porous medium, or Fick's law of diffusion.

This approach has been developed by Cushman and co-workers; see Weinstein *et al.* [26] and references therein, as well as Eringen [27], Schrefler [28], and Zhu *et al.* [29].

None of the aforementioned three classes of models can take into account the effect of the microstructure of a porous medium as it undergoes deformation. Flow and transport processes in any porous medium, deformable or not, are controlled by its morphology that consists of the pore-size distribution and pore connectivity [1,30]. For macroscopic flow and transport processes to occur, there has to be a sample-spanning cluster of connected pores, which exists only if the porosity ϕ of the pore space is larger than a critical porosity, or the percolation threshold. As a porous medium is deformed, its pore space undergoes significant changes. The question is then, does the pore space become better connected or loses its connectivity as the solid matrix deforms?

The question has given rise to a fourth class of models, those that can take into account the effect of the microstructure of a porous medium on its deformation and, hence fluid flow and transport. Thus, there have been some efforts to develop such models and approaches. Zhu and Wang [31] modeled porous media by a simple-cubic network to study fluid flow and dilatancy in a network of microscracks, represented by the network's bonds. Boutt and McPherson [32] used the discrete-element method (see below) to study cracking of rock samples, but did not study fluid flow. Masoud and Alexeev [33] used a random network of filaments in a polymeric matrix, similar to percolation networks with stretching and angle-changing bonds that were studied extensively in the 1980s and 1990s [34,35] (for a comprehensive review see Sahimi [36]) to study the diffusion coefficient and permeance of a deformed polymer network. Jasinski *et al.* [37] studied, both experimentally and by numerical simulations, flow and transport properties of Bentheim sandstones, extending the earlier works of Dautriat *et al.* [38] and Thovert and Adler [39], and similar to the work of Arns *et al.* [40,41]. They [37] discretized the linear elasticity equation and solved it numerically. To do so, the material, represented by a cubic simulation cell, was partitioned into a number of elementary cubes that represented either the solid matrix or the pores. The geometry of the sample was provided by an image obtained through computed microtomography. Each elementary cube was discretized by tetrahedra. The results of the simulations were then compared with the experimental data. Jivkov *et al.* [42] used a three-dimensional (3D) network with a coordination number of up to 14 to study the permeability of samples of rock, but the effect of deformation was not studied.

The focus of this paper is on studying the effect of deformation on fluid flow through a particular class of porous materials, namely, a packing of particles that represent unconsolidated porous media. The advantage of a packing of particles is that much is known about its microstructure [36,43]. Both regular and random packings are studied, and the deformation of the particles is assumed to be small, so that the linear theory of elasticity can be utilized. We use a quasi-static model based on Hertz's contact theory [44] in order to describe the interaction between the particles, report on the various morphological properties of the pore space, as well as its effective permeability as functions of the applied strain and other relevant parameters, and discuss their implications. Our study represents a step toward gaining better understanding of the effect of deformation, caused by a variety of factors, on flow and transport properties of porous media modeled by a packing of particles.

The rest of this paper is organized as follows. In Sec. II we describe an algorithm for generating the granular porous media that we use in the simulations. Section III describes the equation of motion of the particles and numerical simulations of the deformation. In Sec. IV we describe briefly the lattice-Boltzmann method that is used for computing the effective permeability of the deforming pore space. The results are presented and discussed in Sec. V, while the paper is summarized in Sec. VI.

II. GENERATION OF RANDOM PACKINGS

We study deformation and flow in two regular packings, the simple-cubic (SC) and face-centered cubic (FCC) packings, as well as random packings of spherical particles. To generate the random packings, the particles were distributed randomly in a cubic simulation cell. The particles' size followed a Gaussian distribution, and three particle-size distributions were utilized (see below). The boundaries in all the directions were rigid. Initially, there may be overlaps between the particles in the random packing. To eliminate them, the following rearrangement procedure was used. An overlap rate between two particle was defined by [45], $\mathcal{R} = (r_i + r_j - d_{ij})/(r_i + r_j)$, where d_{ij} is the center-to-center distance between particles i and j so that for overlapping particles, $d_{ij} < (r_i + r_j)$. For each particle i a search was conducted to identify those that may have overlap with i. Then, for each overlapping particle j centered at $\mathbf{R}_j$ a new position was calculated by

$$\mathbf{R}_j^{(n)} = \mathbf{R}_j^{(o)} + \left(\frac{r_i + r_j}{d_{ij}}\right)(\mathbf{R}_i^{(o)} - \mathbf{R}_j^{(o)}) \,, \tag{1}$$

where $\mathbf{R}_i$ and $\mathbf{R}_j$ are, respectively, the position vectors of particles i and j along the ray that connects their centers to the origin of the coordinates, and superscripts n and o indicate the new and old vectors. If particle i overlaps with n_i other particles, then Eq. (1) provides n_i positions, and the actual new position of particle i is given by

$$\mathbf{R}_i = \frac{1}{n_i} \sum_{j=1}^{n_i} \mathbf{R}_j^{(n)} \ , \tag{2}$$

where $\mathbf{R}_i^{(n)}$ is calculated by Eq. (1). The relaxation process was applied to every overlapped particle. If a particle neither overlaps nor contacts others, it is moved to contact its nearest neighbor. By iterating the process, the overlap rate $\mathcal{R}$ decreases gradually. To avoid any bias, the sequence of the particle rearrangements is randomized after each iteration. The overlap rate $\mathcal{R}$ eventually drops below a preset threshold, which we took it to be 10^{-3}. Typically, it took about 1500 iterations to remove practically all the overlaps.

In addition to a dense random packing that has a porosity $\phi \approx 0.32$, we also generated a loose random packing with a porosity of 0.54. The generation of the regular FCC and SC packings is trivial and needs no explanation.

III. EQUATIONs OF MOTION AND SIMULATION OF DEFORMATION

The model that we use for the mechanics of the packings is similar to the discrete-element method [46], except that we assume the quasi-static condition in which the displacement field throughout the packing is calculated particle by particle. Under equilibrium condition the governing equation for a particle with N_c contacts is given by

$$\mathbf{F}_{\text{ext}} - \sum_{c=1}^{N_c} \mathbf{F}_c = \mathbf{0} \ , \tag{3}$$

where $\mathbf{F}_{\text{ext}}$ and $\mathbf{F}_c$ are, respectively, the external and contact forces. The contact force is given by

$$\mathbf{F}_c = F_{xc}\mathbf{i} + F_{yc}\mathbf{j} + F_{zc}\mathbf{k} = (F_n e_{ix})\mathbf{i} + (F_n e_{iy})\mathbf{j} + (F_n e_{iz})\mathbf{k} \ , \tag{4}$$

with e_{ix}, e_{iy} and e_{iz} being the component of the unit vector $\mathbf{e}_i$, pointing from the center of a particle i at the spatial position $\mathbf{X}_i$ and pointing toward the center of a particle j with its center's position at $\mathbf{X}_j$, $\mathbf{e}_i = (\mathbf{X}_i - \mathbf{X}_j)/d_{ij}$. Here, F_n is the magnitude of the normal contact force between two particles that, according to Hertz's theory, is given by [44]

$$F_n = \frac{4}{3} Y_e \sqrt{R\delta_n^3} \ , \tag{5}$$

where δ_n is the overlap between two particles in contact, given by

$$\delta_n = r_i + r_j - d_{ij} \ , \tag{6}$$

$$\frac{1}{Y_e} = \frac{1-\nu_i^2}{Y_i} + \frac{1-\nu_j^2}{Y_j} \ , \tag{7}$$

$$\frac{1}{R} = \frac{1}{r_i} + \frac{1}{r_j} \ . \tag{8}$$

Here, R is the relative curvature, Y_i and Y_j are the Young's moduli of the two particles and ν_i and ν_j their Poisson's ratios (if the two particles are made of different materials), and r_i and r_j are the radii of the particles in contact. The normal contact force is first considered, after which the contribution of the tangential (shear) force F_s or the friction force is taken into account. According to the Coulomb's law, one must have

$$F_s \leq \mu F_n \ , \tag{9}$$

where μ is the friction coefficient. All the particles in the packing must satisfy inequality (9). The shear or tangential force is usually written as, $F_s = k_s \delta_s$, with k_s and δ_s being, respectively, the tangential stiffness and displacement.

Computing k_s that enables one to calculate the contribution of the shear force is not straightforward, because it depends, in general, on the *history* of deformation and sliding of one particle on another. On the other hand, such contributions to the deviatoric stress tensor are believed to be small [47] and, therefore, the normal forces contribute most to the tensor. Under such conditions, k_s is computed by [48,49]

$$k_s = \frac{2\mu_e^{2/3}[6(1-\nu_e)RF_n]^{1/3}}{2-\nu_e} \ , \tag{10}$$

where μ_e and ν_e are, respectively, the effective shear modulus and Poisson's ratio, given by,

$$\frac{1}{\mu_e} = \frac{2-\nu_i}{\mu_i} + \frac{2-\nu_j}{\mu_j} \ , \tag{11}$$

$$\frac{2}{\nu_e} = \frac{1}{\nu_i} + \frac{1}{\nu_j} \ , \tag{12}$$

with μ_i being the shear modulus of particle i. Due to the different shear forces exerted on the particles, k_s varies from particle to particle and from one direction to another.

Equation (5) expresses a nonlinear relation between the normal contact force F_n and δ_n, based on which k_n is calculated. To simplify the problem, a linear relationship is assumed

[49] to approximate the nonlinear relation (5), namely, $F_n = k_n \delta_n$, with k_n selected so as to minimize the difference between the assumed linear relation and Eq. (5). Thus, we determine [47] the minimum of the quantity,

$$I^2 = \int_0^{\delta^*} \left(\frac{4}{3} Y_e \sqrt{R\delta_n^3} - k_n \delta_n \right)^2 d\delta_n \ , \tag{13}$$

where δ^* is the average of all particles' overlap. Then, k_n is determined by, $\partial I^2 / \partial k_n = 0$, yielding

$$k_n = \frac{8}{7} Y_e \sqrt{R\delta_f} \ . \tag{14}$$

Note that the normal stiffness k_n is not only a function of a particle's properties, but also the particles' overlaps. One does not have to linearize Hertz' theory and can instead solve the complete nonlinear problem iteratively. Our preliminary simulations with the full nonlinear problem indicated that *for small displacements* (which is assumed in this work) the linearization provides good approximation to the actual nonlinear problem with the error being on the order of a few percent.

We assume that the force-displacement relation follows the Hooke's law [47]. Under the external force applied to the packing, the particles are displaced and deformed. The incremental displacement δu_x in the x direction is then given by

$$\delta u_x = \begin{cases} \dfrac{\sum_c F_{xc}}{k_n + k_s} & \text{if } \frac{k_s}{k_n + k_s} \left| \sum_c F_{xc} \right| < \mu \sqrt{\left(\sum_c |F_{yc}| \right)^2 + \left(\sum_c |F_{zc}| \right)^2} \ , \\ \dfrac{\sum_c F_{xc} \pm \mu \sqrt{(\sum_c |F_{yc}|)^2 + (\sum_c |F_{zc}|)^2}}{k_n} & \text{otherwise .} \end{cases} \tag{15}$$

The sums are over all the contact points. The $\pm$ sign must be selected in such a way that the frictional and active forces are in the directions opposite of each other. In a similar manner, the incremental displacements in the y and z directions are given by

$$\delta u_y = \begin{cases} \dfrac{\sum_c F_{yc}}{k_n + k_s} & \text{if } \frac{k_s}{k_n + k_s} \left| \sum_c F_{yc} \right| < \mu \sqrt{\left(\sum_c |F_{xc}| \right)^2 + \left(\sum_c |F_{zc}| \right)^2} \ , \\ \dfrac{\sum_c F_{yc} \pm \mu \sqrt{\left(\sum_c |F_{xc}| \right)^2 + \left(\sum_c |F_{zc}| \right)^2}}{k_n} & \text{otherwise ,} \end{cases} \tag{16}$$

and

$$\delta u_z = \begin{cases} \dfrac{\sum_c F_{zc}}{k_n + k_s} & \text{if } \frac{k_s}{k_n+k_s}\left|\sum_c F_{zc}\right| < \mu\sqrt{\left(\sum_c |F_{xc}|\right)^2 + \left(\sum_c |F_{yc}|\right)^2}\,, \\ \dfrac{\sum_c F_{zc} \pm \mu\sqrt{\left(\sum_c |F_{yc}|\right)^2 + \left(\sum_c |F_{xc}|\right)^2}}{k_n} & \text{otherwise}\,. \end{cases} \tag{17}$$

It is clear that the displacement of the neighboring contacting particles generates a new nonequilibrium state for a given particle. Thus, the calculations utilized an iterative process in which the forces exerted on a given particle were gradually released until the net force on each particle in the packing was smaller than a threshold. Typically, 150-250 iterations were needed to reach the equilibrium state.

Oedometric compression tests were simulated with both dense and loose packings by imposing various modes of vertical compressive strain on the top boundary. During each compression cycle the bottom face and the lateral boundaries of the system were held fixed. For each strain mode, simulations were carried out to determine the final configuration of the packing. The applied strain was increased up to 3 and 30 percent for the dense and nondense packings, respectively. Once the particles reached their equilibrium state under compression, fluid flow was simulated in the deformed pore space in order to compute the effective permeability and other properties of the pore space as functions of the applied strain. The effective permeability was calculated by the lattice-Boltzmann method, which we describe briefly in the next section.

IV. CALCULATION OF THE EFFECTIVE PERMEABILITY

The effective permeabilities of the three types of packings were calculated using a single-relaxation time lattice-Boltzmann (LB) simulator to simulate fluid flow in the pore space, and invoking Darcy's law to compute the permeability. The flow was assumed to be in the x direction (see Fig. 2 below). The no-slip boundary condition was imposed on the fluid-solid interface, as well as the rigid outer walls of the system (in the y and z directions) by using the standard bounce-back method, and a constant pressure gradient was applied in the flow direction. The computational domain for the flow calculations consisted of $N \times N \times N$ grid points, which must be resolved enough that the effective permeability would not change if a more resolved grid is used. Thus, we carried out a series of preliminary simulations with $N = 100,\ 150,\ 200,\ 225$ and 250 in order to determine an adequate resolution for the computational grid. The results

are shown in Fig. 1, where the relative error is defined by, error $= |K_N - K_{250}|/K_{250}$, with K_N being the effective permeability computed with a grid of size N^3, and K_{250} representing the calculated permeability with the most resolved grid of linear size $N = 250$. Figure 1 indicates that the relative error between the results for $N = 200$ and $N = 250$ is essentially zero. Thus, all the results presented below were obtained with a grid of size 200^3.

The LB simulator uses an iterative sequence of propagations and collisions of fictitious particles at the grid points of the discretized domain. The mass density of each grid point that does not belong to the solid matrix is defined by a set of scalar particle distribution functions $f(x,t)$, each of which is related to a lattice velocity unit vector. At each time step, the particle distribution functions are shifted to neighboring grid points according to their unit velocity vector through the propagation step, also called streaming. Following each streaming step, a collision operation is carried out to update each distribution. The simplest form of the collision operator is based on the Bhatnagar-Gross-Krook (BGK) approximation [50]. The streaming and collision of the fictitious particles are described by the following equation for the particle distribution function f_i [51]:

$$f_i(\mathbf{x} + \mathbf{e}_i \triangle t, t + \triangle t) - f_i(\mathbf{x}, t) = -\frac{1}{\tau_R}[f_i(\mathbf{x}, t) - f_i^{\mathrm{eq}}(\mathbf{x}, t)] \ , \tag{18}$$

where Δt represents the time step in lattice units, τ_R is the dimensionless relaxation time, and $\mathbf{e}_i$ are the velocity basis vectors. The left side of Eq. (18) represents the streaming step by which the particle distribution functions are shifted based on the velocities, while the right side describes the collision operation. The equilibrium distribution f_i^{eq} is given by [52],

$$f_i^{\mathrm{eq}} = \rho \omega_i \left[1 + \frac{3}{c^2}(\mathbf{e}_i \cdot \mathbf{v}) + \frac{9}{2c^4}(\mathbf{e}_i \cdot \mathbf{v})^2 - \frac{3}{2}v^2 \right] \ , \tag{19}$$

where $c = \Delta x/\Delta t$ is the lattice speed, Δx is the grid spacing, $\mathbf{v}$ is the velocity field, ρ the fluid's density, and ω_i are the weight coefficients. We use the standard D3Q19 LB model for 3D modeling [52], for which $\omega_i = 1/18$ for $i = 1,\ 2, \cdots, 6$, $\omega_i = 1/36$ for $i = 7,\ 8, \cdots, 18$ and $\omega_i = 1/3$ for $i = 19$. The fluid density is given by [53], $\rho = \sum_i f_i$, the velocity by, $\rho \mathbf{v} = \sum_i \mathbf{e}_i f_i$, and pressure by, $P = \rho c_s^2$, where c_s denotes the speed of sound in lattice units (equal to $c/\sqrt{3}$). The kinematic viscosity ν is the given by, $\nu = (\tau_R - 0.5)c_s^2$. Low-Mach number Ma flow is simulated with $\mathrm{Ma} = v/c_s \ll 1$. We used a relaxation parameter $\tau_R = 1$. Stewart *et al.* [54] showed that if the relaxation parameter deviates from unity, the resulting permeabilities are not accurate.

Thus, after the porous medium attained its equilibrium state for any given strain, the LB model of fluid flow was used in combination with the Darcy's law

$$\langle v \rangle = -\frac{K}{\eta} \boldsymbol{\nabla} P = -\frac{K}{\eta} \frac{\partial P}{\partial x} \,, \tag{20}$$

in order to calculate the effective permeability K of the deformed porous medium for the corresponding strain, where $\langle v \rangle$ denotes the volume-averaged flow velocity, and η is the fluid's dynamic viscosity. As the Darcy's law is accurate only for creeping flows, all the simulations were carried out for Reynolds numbers $\mathrm{Re} < 1$.

We carried out extensive simulations for packings made of two types of particles, soft and hard. The Young's modulus, shear modulus and Poisson's ratio of the soft particles were 2.7 GPa, 0.97 GPa and 0.42, whereas those for the hard particles were 110 GPa, 44 GPa and 0.24. These are in the range of properties reported for clay particles. Typically, we simulated a packing with about 1500 - 2000 particles. The cubic domain of the packings had dimensions of 8.5 cm, 7.5 cm, 8.14 cm and 8 cm for nondense random packing, dense random packing, and SC and FCC packings, respectively. The sizes of the particles in the random packing were not equal, but followed a Gaussian distribution. Three particle-size distributions were utilized with an average of 3.7 mm and standard deviations of 0.2 mm, 0.3 mm and 0.5 mm. The size of the particles in the regular packings was 3.7 mm. Figure 2 presents the three particle-size distributions that we utilized in the simulations of the random packings, along with a typical configuration of a deformed packing. In the figures described and discussed below, we refer to the three particle-size distributions as PSD1, PSD2, and PSD3. Unless specified otherwise, in all cases the friction factor was assumed to be 0.03.

V. Results and Discussion

In a dense regular packing of particles with equal sizes, the particles move only in the loading direction under the oedometric compression. As a result, the strain field in the packing is almost uniform everywhere. The entire porous medium deforms as a continuous homogeneous material. In addition, the identical spheres rearrange themselves in a crystallike formation when an external force is applied to the packing. In other words, the particles move homogeneously due to the application of the external force. Consequently, the deformation of the regular packing of equal-size particles is due mainly to the local deformation at the particle contact points, rather than being due to particles' relocation.

In the case of random packings, however, the particles move in various directions when an external force is applied. The strain field is not uniform even if the external force is, as in the oedometric compression that we simulate. This effect is particularly significant for particles that are located close to the system's boundary. Thus, the deformation of the particles in the random packing is due to their rearrangement, as well as the local deformation at the contact points. In what follows we present the results and discuss their implications.

A. Distributions of the pores' size and length

One of the most interesting properties of the packings of particles as they undergo deformation is the change in their pore-size distribution (PSD) and pore-length distribution (PLD), which directly affect their effective permeability and porosity. Thus, we first calculated the PSD and PLD of the pore space of the random packings. To do so, a well-known result [55] was used to map the pore space between the particles onto an equivalent 3D Voronoi network in which the bonds of the network, representing the flow channels between the particles, are the edges of the Voronoi polyhedra. To carry out the mapping, we first used [56,57] the Delaunay tessellation to divide the packing into cells of four nearest neighbor particles, with each cell being a tetrahedron with its four vertices located at the particles' centers in the cell. Access to this void region is through any of the four surfaces that are created by three particles in the cell. Since the vertices of the tetrahedron are the same as the particles' centers, the void projected onto each of the four faces indicates the smallest cross section perpendicular to the flow field that would be accessible for fluid flow into the central void space of the cell. Due to the random structure of the packing, the sizes and shapes of such cross sections vary in space.

Delaunay tessellation is the geometric dual of the Voronoi tessellation [58]. The Voronoi cells are polyhedra, each of which contains exactly one particle of the packing, such that any point within every polyhedron is closer to that particle's center than the center of any other particle in the packing. Hence, the Delaunay tessellation is used to construct a network that represents the solid phase of the random packing, whereas the Voronoi tessellation is utilized for constructing the pore network equivalent of the void space. The vertices of the Voronoi polyhedra are connected by the edges of the polyhedra that represent the pore space.

To construct the Voronoi network, the positions of network's vertices are identified and, given the four particles that surround each vertex, the way the vertices are connected to each

other are determined. For each particle, referred to as the main particle, all the possible nearest-neighbor groups of particles are considered. Then, for each group a point is located that has the same distance from the four particles' centers, which will be a vertex of the Voronoi network *if and only if* its distance from the center of the main particle is equal to, or less than, its distance from the other particles' centers in the packing. Otherwise, such a group of four particles cannot generate a Delaunay cell, and that point cannot be a vertex in the Voronoi network. The procedure is repeated for all the particles in the packing, so that the spatial coordinates of all the Voronoi vertices around each main particle, as well as the groups of four particles that generate each Delaunay cell, are determined.

After constructing the Voronoi network, we determined the effective length and radius of each bond (pore throat) in the network. As pointed out earlier, the cross sections of the void space representing the flow channels vary along their length. The length of each bond of the Voronoi network was calculated by using the spatial coordination of its two end sites. To calculate the effective radius of each pore throat, we define a hydraulic diameter D_h for each bond by the classical relation,

$$D_h = 2\,\frac{\text{flow cross section}}{\text{wetted perimeter}}\,.$$

Simple geometrical analysis, together with the spatial coordinates of the particles' centers in the random yield the flow cross sections and the wetted perimeters.

In what follows when we refer to the PSDs and the PLDs after deformation, we mean those at the maximum applied strain. Figure 3 presents the calculated PSDs of the three dense packings of hard particles for which the particle-size distributions are shown in Fig. 2. The results are for before and after deformation. Only the packing with the broadest particle-size distribution, the PSD3, exhibits some change in its pore-size distribution after deformation. This is understandable as the particles are hard, and the packings are dense. Figure 4 shows the corresponding PLDs. In this case the differences in the PLDs before and after deformation are relatively significant, since the hard particles may not deform much, but can move significantly under compression.

Figure 5 shows the computed PSDs of the three dense packings of soft particles, before and after deformation, with the particle-size distributions shown in Fig. 2. Once again, only the packing with the broadest particle-size distribution exhibits some change in its PSD after

deformation. This indicates that it is the high density of the particles, rather than the rigidity of the particles, that is responsible for the changes in the PSDs. The corresponding PLDs are presented in Fig. 6. The magnitude of the differences in the PLDs before and after deformation is comparable to those for the packings of the hard particles, hence confirming our assertion that it is the particle density that plays the most important role in the deformation process that we have simulated.

Next, we present the results for a random packing with a porosity of 0.54. Figure 7 depicts the computed PSDs of the three random packings of hard particles, before and after deformation. Relative to the dense packings, the changes in the PSDs are more pronounced. The changes in the PLDs are even clearer; see Fig. 8. This is understandable because the higher porosity of the packings allows the particles to move farther after the external strain is applied.

Similarly, if the random packings with a porosity of 0.54 consist of soft particles, then, the changes in their PSDs and PLDs are even larger after deformation, as shown, respectively, in Figs. 9 and 10. Note that in all the cases, the deformation gives rise to a larger number of shorter pore throats than those in the packings before the deformation. The significant changes in the distribution of the pore lengths also affect the permeability of the packings after deformation. This will be discussed shortly.

B. Porosity

The effect of deformation on the porosity is also important. The change in the porosity does depend, of course, on the stiffness of the particles and their size distribution. Figure 11 presents the fluctuations in the porosities of the dense random packings with the particle-size distribution PSD3 in two directions, namely, in the flow direction x, and in the z direction along which the external strain was applied. They represent the porosities in the planes perpendicular to the given directions, and indicate that the deformation propagates well throughout the packings. Similar results were obtained for other types of packings.

Figure 12 presents the strain-dependence of the porosity of the dense packings with the two types of particles, soft and hard, and their three size distributions shown in Fig. 2. In this figure and in the following the porosity is normalized with respect to its value before deformation. In the case of a narrow particle-size distribution the porosity is reduced by only about 5 percent at the maximum strain applied, with the change being even smaller if the particles are hard.

The reduction in the porosity rises to about 7 percent with the widest particle-size distribution (PSD3 in the figure). As expected, the change in the porosity is larger when the particles are soft. Similar behavior is obtained if we use regular packings of particles.

The reduction in the porosity is, however, significantly higher in a random packing with an initial porosity of 0.54. Figure 13 presents the results for the two types of particles and the three particle-size distribution of Fig. 2. Even in the packing of the hard particles the porosity at the maximum strain has been reduced by as much as 20 percent. The reduction in the porosity is even larger in the case of regular packings; see Fig. 14 where we show the results for the SC and FCC lattices. This is perhaps expected as the regular arrangement of the particles is more amenable to deformation and rearrangement than those of a random packing of the particles.

We find that in the case of nondense packing, as well as the regular ones, the changes in the porosity follow a power law in the applied strain S,

$$\frac{\phi}{\phi_0} - 1 = -nS^m \,, \tag{21}$$

where ϕ_0 is the initial porosity before deformation. Estimates of n and m are listed in Table I. Figures 13 and 14 also show the fits. The coefficient n is, of course, nonuniversal. For loose random packings of hard particles, $m \approx 1.9 \pm 0.1$, whereas with soft particles, $m \approx 1.5 \pm 0.07$, for the SC packings, $m \approx 1.23 \pm 0.05$, and $m \approx 1.54$ and 1.35 for the FCC packings with hard and soft particles, respectively. Thus, the exponent m is also nonuniversal among the various types of packings. In the case of the dense packings the porosity decreases with the strain essentially linearly, so that, $m = 1$. Estimates of the coefficient n for the various dense packings are also listed in Table I, while Figs. 12 also show the fits.

C. Number of contacts between particles

The mean number of contacts C, defined as the number of spheres that any particle touches, is an important characteristic of a deforming packing. Figure 15 presents the results for the dense packing of soft particles, as well as the packing with a porosity of 0.54. As the external strain increases, so also does the number of contacts. For identical strains the increases are smaller in the case of the nondense random packing due to the larger void space in the system.

During the initial stages of compressing the loose packings, the particles are mostly displaced in the large void space of the packings. So, the number of the contacts between the particles

does not change rapidly, giving rise to the concave dependence of the contact on the strain seen in Fig. 15. The slope of the plot is also higher at higher strain modes. In other word, the rate of increase of the contact number is higher at larger strains. The dense packing produces the convex dependence of the dependence of the contact number on the strain. At the initial stages of compression, the contact number increase rapidly because the packing is dense and the particles come into contact easily. When the strain takes on higher values, the packing becomes very compact, leaving not enough void space for the particles to move freely and, thus, the rate of the increase of the contact number is lower at higher strain modes.

D. Fluid stress distribution and deformation

An important characteristic of fluid flow through a deforming porous medium is the distribution of the stresses that are exerted by the fluid inside the pore space and its evolution with the deformation. As long as the morphology of the porous medium, the flow regime, and the type of the fluid (Newtonian versus non-Newtonian) do not change, the shape of the distribution would remain the same. But, because deformation changes the morphology, any change in the stress distribution would also be a reflection of the deformation. To calculate the stress distribution, we computed the second-rank stress tensor induced by fluid flow in the pore space, before and after deformation. The stress tensor $\boldsymbol{\tau}$ is given by

$$\boldsymbol{\tau} = \frac{1}{2}\eta \left[\boldsymbol{\nabla}\mathbf{v} + (\boldsymbol{\nabla}\mathbf{v})^{\mathrm{T}} \right] , \tag{22}$$

where the notation is the same as before, and superscript T denotes the transpose operation. The eigenvalues of the tensor were then computed, with the largest one being the most important flow-induced stress [59,60]. We then calculated the distribution of the largest eigenvalues.

Since we wish to construct a probability distribution function (PDF) for the calculated stresses that is hopefully applicable to other types of porous media, we normalize the stresses, $\tau^* = (\tau - \langle\tau\rangle)/\sigma$, where $\langle\tau\rangle$ is the mean stress, and σ is the standard deviation. Figure 16 presents the stress distribution in the dense packings of soft particles before deformation and after the maximum strain was applied. The particles' sizes were distributed according to the three distributions shown in Fig. 2. The shape of the distribution suggests that it may be fit to a log-normal distribution. Suppose that the mean and standard deviation of the PDF of the un-normalized ln(stress) are, respectively, m and σ, so that we denote the distribution by

$\ln \mathcal{N}(m, \sigma)$. Then, the PDF of τ^* is a three-parameter distribution $\ln \mathcal{N}(\gamma^*, m^*, \sigma)$ given by [60]

$$h(\tau^*) = \frac{1}{\sqrt{2}\sigma\pi(\tau^* - \gamma^*)} \exp\left\{ -\frac{1}{2}\left[\frac{\ln(\tau^* - \gamma^*) - m^*}{\sigma} \right]^2 \right\} , \tag{23}$$

where $m^* = m - \ln \sigma_\tau$, and $\gamma^* = -\langle \tau \rangle / \sigma$, with $\sigma_\tau = \exp(m + \sigma^2/2)\sqrt{\exp(\sigma^2) - 1}$. Note that γ^* represents the minimum value of the normalized stress. As Fig. 16 indicates, Eq. (23) provides reasonably accurate representation of the numerical data. Given the dense structure of the packings, the stress distribution changes somewhat more significantly only in the pore space with the widest particle-size distribution.

Figure 17 presents the same, but for the random packings with an initial porosity of 0.54. Due to the larger void space in the packings and, therefore, more significant deformation of the particles, the changes in the PDF of the stresses are much larger than those in the dense packings. Note also that the range of the stresses exerted on the pore space with the wider particle-size distribution is broader in the loose packings than the dense ones. In addition, in both types of the packings the stress distributions in the undeformed state are more sharply peaked. This is, of course, due to pore closure or significant reduction in the pore sizes, on the one hand, and opening up other pores, on the other hand, both caused by deformation.

In Fig. 18 we present the corresponding results for the FCC and SC packings. In these cases the distributions are no longer as sharply peaked as those in the random packings. The reason is that the regular structure of the FCC and SC packings gives rise to broader distribution of the local flow velocities and, therefore, broader distribution of the stresses. Although the fit of the numerical results to the long-normal distribution is not as accurate as those for the random packings, Eq. (23) does provide a reasonable description of the stresses.

The fact that in all the cases the stress distribution can be accurately represented by a log-normal PDF is significant. The long tail of the distribution implies that there is a small but significant fraction of the pore space in which very large stresses exist. This, of course, has direct implications for the solid phase as well, because if the stress in the fluid in the vicinity of the solid surface is large, it directly affects the surface. On the other hand, the sharp and narrow peaks of the distributions imply that a large fraction of the pore space experience small stresses, implying that the internal solid surface in that part of the pore space also experiences small stress. Another characteristic of log-normal distribution is their variance, which means

that there are wide fluctuations in the stresses.

E. Effective permeability

Figure 19 presents the strain-dependence of the permeabilities of the dense packings with the two types of particles, soft and hard, in which the size of the particles is distributed according to the particle-size distributions of Fig. 2. The permeabilities are normalized with respect to their values before deformation. The results indicate several important features:

(i) The reduction in the permeabilities is *not* a strong function of the elastic moduli of the particles.

(ii) Even though the final applied strain is only 0.03, the reductions in the permeabilities are very significant, whereas as Figs. 12 and 13 indicate, the corresponding reductions in the porosities are much smaller.

(iii) The change in the permeabilities is also *not* a strong function of the particle-size distribution.

These features are due to the dense structure of the packings. As a result of applying an external strain to the top surface of the system, the deformation propagates significantly toward the lower part of the packings, resulting in the reduction in the permeability.

Figure 20 presents the dependence of the normalized permeabilities on the porosities for the dense packings. If we replot the normalized permeability data shown in Fig. 20 versus the normalized porosities, all the three curves collapse onto each other. This is shown in Fig. 21.

The results for the strain-dependent permeability of the random loose packings with a porosity of 0.54 are presented in Fig. 22. Note that the final applied strain to the packings is ten times larger than that in the dense packings. In this case the differences between the permeabilities of the packings with hard and soft particles are larger at larger strains, because the larger void space of the packings allows larger deformation of the soft particles. Given that the initial porosity is large, the reduction in the permeability is even larger than the dense counterpart. Figure 23 depicts the corresponding porosity-dependent permeabilities. Once again, the numerical data collapse onto a single curve, if the normalized permeability is plotted versus the normalized porosity. This is shown in Fig. 24. The data collapse implies that the relative reduction of the permeability is a universal function of the relative reduction in the porosity, independent of the particle-size distribution.

The results for the SC and FCC packings, shown in Fig. 25, indicate even larger reduction in the permeabilities. Due to their dense structure, the changes in the permeability of both regular packings are not sensitive to the elastic modulus of the particles.

The conclusions are that, (i) in all the case the reduction in the permeabilities vary essentially linearly with the applied strain; (ii) while the change in the permeability is not a strong function of the hardness of the particles, it depends strongly on the initial morphology of the pore space, and (iii) the normalized permeability is a universal function of the normalized porosity, independent of the particle-size distribution.

F. Effect of the friction coefficient

As already pointed out, larger friction between the particles leads to smaller deformation in them. Thus, we expect greater reduction in the permeability when the friction coefficient is smaller. This is borne out by the results shown in Fig. 26, which presents the results for the permeability and porosity for two friction coefficients in a loose packing.

VI. Summary

Extensive numerical simulations were carried out to study the effect of deformation on the morphological and flow properties of packed beds of spherical particles, when they are under mechanical compaction. Both random and regular packings of particles were studied. The deformation leads to the closure of some pores and opening up of others and, therefore, the resulting reduction in the permeability varies from relatively small to large, depending on the morphology of the initial pore space. The distribution of the pores' lengths, the porosity of the pore space, and the pore-size distribution also evolve under an external strain. It is of course the changes in the morphology of the pore space that lead to the strong reduction of the permeability.

The Kozeny-Carman (KC) equation [61,62],

$$K = \frac{\langle D \rangle^2}{36 C_{\rm KC}} \, \frac{\phi^3}{\mathcal{T}^2 (1-\phi)^2} \tag{24}$$

is often used to correlate the permeability of packed beds of particles with their porosity ϕ, where $\langle D \rangle$ is the mean particle diameter, $\mathcal{T}$ is the volume-averaged tortuosity, and $C_{\rm KC}$ is the Kozeny-Carman shape factor that depends on the materials that the particles are made of,

and accounts for the variations in the permeability of porous media having the same porosity, but distinct microstructures. C_{KC} is usually taken to be 2.5 for packings of spherical particles. The tortuosity can be defined in a variety of ways [63,64]. We find, however, that if the KC equation is to be used to correlate the permeability with the porosity ϕ of the deforming pore space, C_{KC} must depend on ϕ. This will, however, be purely empirical, as a result of which the equation loses its predictive power.

Acknowledgments

S.B. is grateful to the Mork Family Department of Chemical Engineering and Materials Science at the University of Southern California for a doctoral fellowship. This research was supported as part of the Center for Geologic Storage of CO_2, an Energy Frontier Research Center funded by the U.S. Department of Energy (DOE), Office of Science, Basic Energy Sciences (BES), under Award number DE-SC0C12504.

Table I. Numerical values of the exponent m and the prefactor n [see Eq. (21)] for various types of packings, particle-size distributions, and type of particles (soft and hard).

Loose random and regular		
Packing	m	n
PSD1-hard	2.00	2.24
PSD2-hard	1.89	2.00
PSD3-hard	1.83	1.90
PSD1-soft	1.57	1.45
PSD2-soft	1.47	1.40
PSD3-soft	1.43	1.39
SC-hard	1.28	1.13
SC-soft	1.18	1.12
FCC-hard	1.54	5.92
FCC-soft	1.35	4.96
Dense		
PSD1-hard	1.0	1.56
PSD2-hard	1.0	1.60
PSD3-hard	1.0	1.61
PSD1-soft	1.0	1.89
PSD2-soft	1.0	2.10
PSD3-soft	1.0	2.18

[1] M. Sahimi, *Flow and Transport in Porous Media and Fractured Rock*, 2nd ed. (Wiley-VCH, Weinheim, 2011).

[2] E. Iritani, N. Katagiri, K. Yamaguchi, and J.-H. Cho, Compression-permeability properties of compressed bed of superabsorbent hydrogel particles, Drying Technol. **24**, 1243 (2006).

[3] E. Karada, Investigation of swelling/sorption characteristics of highly swoolen AAm/AMPS hydrogels and semi IPNs with PEG as biopotential sorbent, J. Encapsulation Adsorption Sci. **1**, 6 (2010).

[4] Q. Wu, Y. Andreopoulos, S. Xanthos, and S. Weinbaum, Dynamic compression of highly compressible porous media with application to snow compaction, J. Fluid Mech. **542**, 281 (2005).

[5] A. Carbone, B.M. Chiaia, B. Frigo, and C. Türk, Snow metamorphism: A fractal approach, Phys. Rev. E **82**, 036103 (2010).

[6] J. Ghassemzadeh and M. Sahimi, Pore network simulation of fluid imbibition into paper during coating - III: modeling of two-phase flow, Chem. Eng. Sci. **59**, 2281 (2004).

[7] R. Masoudi and K.M. Pillai, Darcy's law-based model for wicking in paper-like swelling porous media, AIChE J. **56**, 2257 (2010).

[8] H. Salimi, A. Pourjavadi, F. Deidi, P. Eftekhar Jahromi, and R. Soleyman, New smart carrageenan-based superabsorbent hydrogel hybrid: Investigation of swelling rate and environmental responsiveness, J. Appl. Polymer Sci. **117**, 3228 (2010).

[9] M.T. Savoji and A. Pourjavadi, Partially hydrolized kappa carrageenan - polyacrylonitrile as a novel biopolymer-based superabsorbent hydrogel: synthesis, characterization and swelling behavior. Polymer Eng. Sci. (2006).

[10] M. Sahimi and A.O. Imdakm, Hydrodynamics of particulate motion in porous media, Phys. Rev. Lett. **66**, 1169 (1991).

[11] P. Meakin, *Fractals, Scaling and Growth far from Equilibrium* (Cambridge University Press, London, 1998).

[12] W. Lai and V.C. Mow, Drag-induced compression of tissues around a diarthrodial joint, Biorheology **17**, 111 (1980).

[13] S.A. Koehler, S. Hilgenfeldt, and H.A. Stone, A generalized view of foam drainage: Experiment and theory, Langmuir **16**, 6327 (2000).

[14] S. Hutzler, N. Péron, D. Weaire, and W. Drenckhan, The foam/emulsion analogy in structure and rainage. Euro. Phys. J. E **14**, 381 (2004).

[15] O. Pitois, E. Lorenceau, N. Louvet, and F. Rouyer, Specific surface area model for foam permeability, Langmuir **25**, 97 (2009).

[16] E. Lorenceau, N. Louvet, F. Rouyer, and O. Pitois, Permeability of aqueous foams, Euro. Phys. J. E **28**, 293 (2009).

[17] M. Leonowicz and D. Oleszak, Kinetics of swelling and drug release from PNIPAAm/Aliginate stimuli responsive hydrogels, Solid State Phenomena **154**, 17 (2009).

[18] M. Biot, General theory of three dimensional consolidation, J. Appl. Phys. **12**, 155 (1941).

[19] M. Biot, Theory of deformation of a porous viscoelastic anisotropic solid, J. Appl. Phys. **27**, 459 (1956).

[20] O. Iliev, A. Mikelić, and P. Popov, On upscaling certain flows in deformable porous media, Multiscale Model. Simul. **7**, 93 (2008).

[21] S. Whitaker, *The Method of Volume Averaging* (Kluwer Academic, Dordrecht, 1999).

[22] D.L. Koch and J.F. Brady, Dispersion in fixed beds, J. Fluid Mech. **154**, 399 (1985).

[23] S.M. Hassanizadeh and W.G. Gray, General conservation equations for multi-phase systems: 1. Averaging procedure, Adv. Water Resour. **2**, 131 (1979).

[24] S.M. Hassanizadeh and W.G. Gray, General conservation equations for multi-phase systems: 2. Mass, momenta, energy, and entropy equations, Adv. Water Resour. **2**, 191 (1979).

[25] S.M. Hassanizadeh and W.G. Gray, Mechanics and thermodynamics of multiphase flow in porous media including interface boundaries. Adv. Water Resour. **13**, 169 (1990).

[26] T.F. Weinstein, L.S. Bennethum, and J.H. Cushman, Two-scale, three-phase theory for swelling drug delivery systems. Part I: Constitutive theory. J. Pharmaceutical Sci. **97**, 1878 (2008).

[27] A.C. Eringen, A continuum theory of porous elastic solids, Int. J. Eng. Sci. **32**, 1337 (1994).

[28] B.A. Schrefler, Mechanics and thermodynamics of saturated/unsaturated porous materials and quantitative solutions, Appl. Mech. Rev. **55**, 355 (2002).

[29] H. Zhu, A. Dhall, S. Mukherjee, and A.K. Datta, A model for flow and deformation in unsaturated swelling porous media, Transp. Porous Media **84**, 335 (2010).

[30] M. Sahimi, Flow phenomena in rocks: from continuum models to fractals, percolation, cellular automata and simulated annealing, Rev. Mod. Phys. **65**, 1393 (1993).

[31] W. Zhu and T.-F. Wong, Network modeling of the evolution of permeability and dilatancy in compact rock, Water Resour. Res. **104**, 2963 (1999).

[32] D.F. Boutt and B.J.O.L. McPherson, Simulation of sedimentary rock deformation: Lab-scale model calibration and parameterization, Geophys. Res. Lett. **29**, 1954 (2002).

[33] H. Masoud and A. Alexeev, Permeability and diffusion through mechanically deformed random polymer networks, Macromolecules **43**, 10117 (2010).

[34] S. Arbabi and M. Sahimi, Mechanics of disordered solids. I. Percolation on elastic networks with central forces, Phys. Rev. B **47**, 695 (1993).

[35] M. Sahimi and S. Arbabi, Mechanics of disordered solids. II. Percolation on elastic networks with bond-bending forces, Phys. Rev. B **47**, 703 (1993).

[36] M. Sahimi, *Heterogeneous Materials I* (Springer, New York, 2003).

[37] L. Jasinski, D. Sangaré, P.M. Adler, V.V. Mourzenko, J.-F. Thovert, N. Gland, and S. Békri, Transport properties of a Bentheim sandstone under deformation, Phys. Rev. E **91**, 013304 (2015).

[38] J. Dautriat, N.F. Gland, S. Youssef, E. Rosenberg, S. Bekri, and O. Vizika-Kavvadias, Stress-dependent directional permeabilities of two analog reservoir rocks: A prospective study on contribution of μ-tomography and pore network models, SPE Res. Eval. Eng. **12**, 297 (2009).

[39] J.-F. Thovert and P.M. Adler, Grain reconstruction of porous media: Application to a Bentheim sandstone, Phys. Rev. E **83**, 056116 (2011).

[40] C.H. Arns, M.A. Knackstedt, W.V. Pinczewski, and W.B. Lindquist, Accurate computation of transport properties from microtomographic images, Geophys. Res. Lett. **28**, 3361 (2001).

[41] C.H. Arns, M.A. Knackstedt, W.V. Pinczewski, and E. Garboczi, Computation of linear elastic properties from microtomographic images: Methodology and agreement between theory and experiment, Geophys. **67**, 1396 (2002).

[42] A.P. Jivkov, C. Hollis, F. Etiese, S.A. McDonald, and P.J. Withers, A novel architecture for pore network modeling with applications to permeability of porous media, J. Hydrol. **486**, 246 (2013).

[43] S. Torquato, *Random Heterogeneous Materials* (Springer, New York, 2002).

[44] K.L. Johnson, *Contact Mechanics* (Cambridge University Press, Cambridge, 1985)

[45] D. He, N.N. Ekere, and L. Cai, Computer simulation of random packing of unequal particles, Phys. Rev. E **60**, 7098 (1999).

[46] *Discrete-Element Modeling of Granular Materials*, Edited by F. Radjaï and F. Dubois (Wiley, Hoboken, 2011).

[47] Z. Lu, M. Abdou, and A. Ying, 3D micromechanical modeling of packed beds, J. Nuclear Mater. **299**, 101 (2001).

[48] R.D. Mindlin, Compliance of elastic bodies in contact, J. Appl. Mech. **16**, 259 (1949).

[49] R.D. Mindlin and H. Deresiewicz, Elastic spheres in contact under varying oblique forces, J. Appl. Mech. **20**, 327 (1953).

[50] P.L. Bhatnagar, E.P. Gross, and M. Krook, A model for collision processes in gases. I. Small amplitude processes in charged and neutral one-component systems, Phys. Rev. **94** 511 (1954).

[51] Z. Guo, B. Shi, and N. Wang, Lattice BGK model for incompressible Navier-Stokes equation, J. Comput. Phys. **165**, 288 (2000).

[52] Y.H. Qian, D. d'Humieres, and P. Lallemand, Lattice BGK models for Navier-Stokes equation, Europhys. Lett. **17**, 479 (1992).

[53] S. Chen and G.D. Doolen, Lattice Boltzmann method for fluid flows, Annu. Rev. Fluid Mech. **30**, 329 (2003).

[54] M.L. Stewart, A.L. Ward, and D.R. Rector, A study of pore geometry effects on anisotropy in hydraulic permeability using the lattice-Boltzmann method, Adv. Water Resour. **29**, 1328 (2006).

[55] A.R. Kerstein, Equivalence of the void percolation problem for overlapping spheres and a network problem, J. Phys. A *16*, 3071 (1983).

[56] S.L. Bryant, P.R. King, and D.W. Mellor, Network model evaluation of permeability and spatial correlation in real random sphere packing, Transp. Porous Media *11*, 53 (1993).

[57] M. Dadvar and M. Sahimi, Pore network model of deactivation of immobilized glucose isomerase in packed-bed reactors. III: Multiscale modeling, Chem. Eng. Sci. **58**, 4935 (2003).

[58] D.F. Watson, Computing the n-dimensional Delaunay tessellation with application to Voronoi polytopes, Comp. J. *24*, 167 (1981).

[59] B. Porter, R. Zauel, H. Stockman, R. Guldberg, and D. Fyhrie, 3-D computational modeling of media flow through scaffolds in a perfusion bioreactor, J. Biomech. **38**, 543 (2005).

[60] N.H. Pham, R.S. Voronov, N.R. Tummala, and D.V. Papavassiliou, Bulk stress distributions in the pore space of sphere-packed beds under Darcy flow conditions, Phys. Rev. E **89**, 033016 (2014).

[61] J. Kozeny, Ueber kapillare Leitung des Wassers im Boden, Sitzungsber Akad. Wiss. Wien **136**, 271 (1927).

[62] P.C. Carman, Fluid flow through granular beds, Trans. Inst. Chem. Eng. London **15**, 150 (1937).

[63] B. Ghanbarian, A.G. Hunt, R.P. Ewing, and M. Sahimi, Tortuosity in porous media: A critical review, Soil Sci. Soc. Am. J. **77**, 1461 (2013).

[64] B. Ghanbarian, A.G. Hunt, M. Sahimi, R.P. Ewing, and T.E. Skinner, Percolation theory generates a physically based description of tortuosity in saturated and unsaturated porous media, Soil Sci. Soc. Am. J. **77**, 1920 (2013).

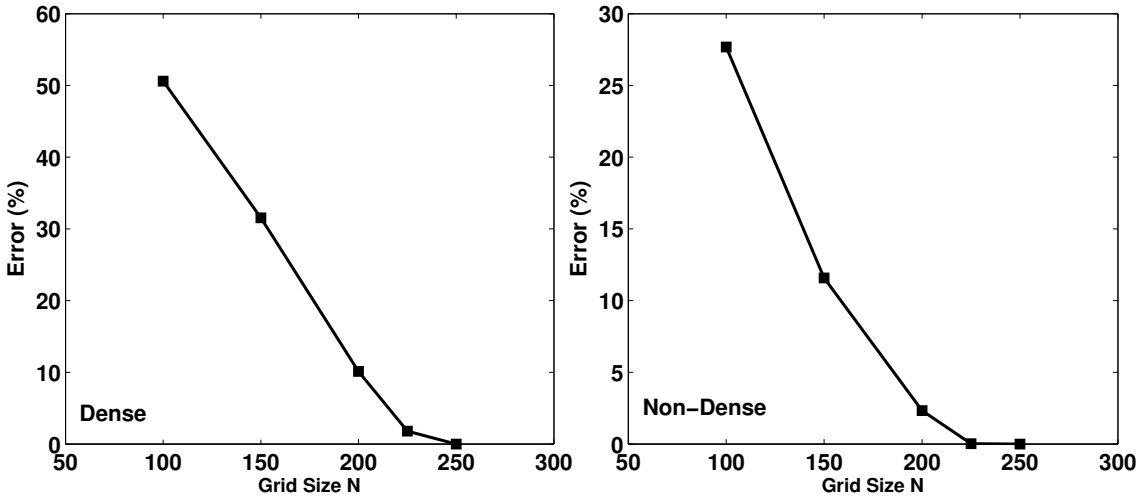

Figure 1: The error, $|K_N - K_{250}|/K_{250}$ in calculating the effective permeability K_N of a grid of size $N \times N \times N$ relative to K for $N = 250$.

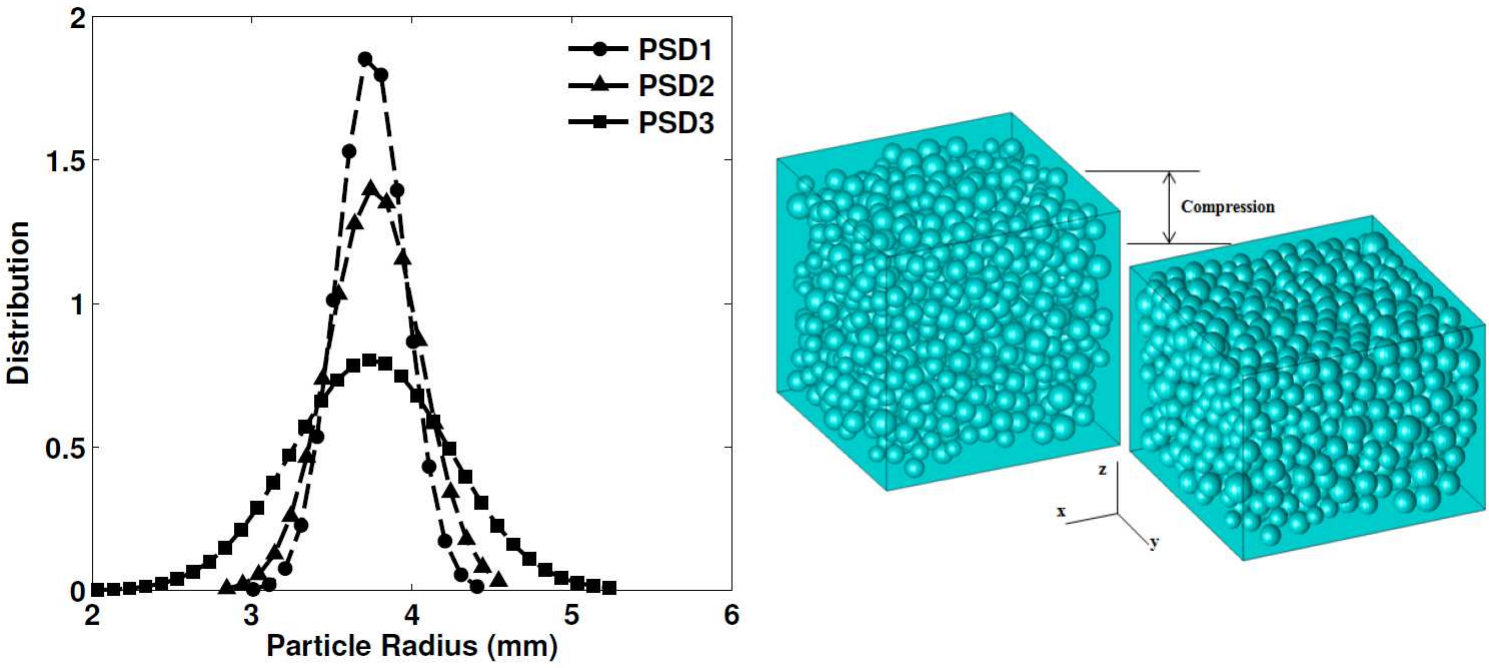

Figure 2: The three particle-size distribution (PSD) used in the for random packings, along with an example of a random packing before and after compression.

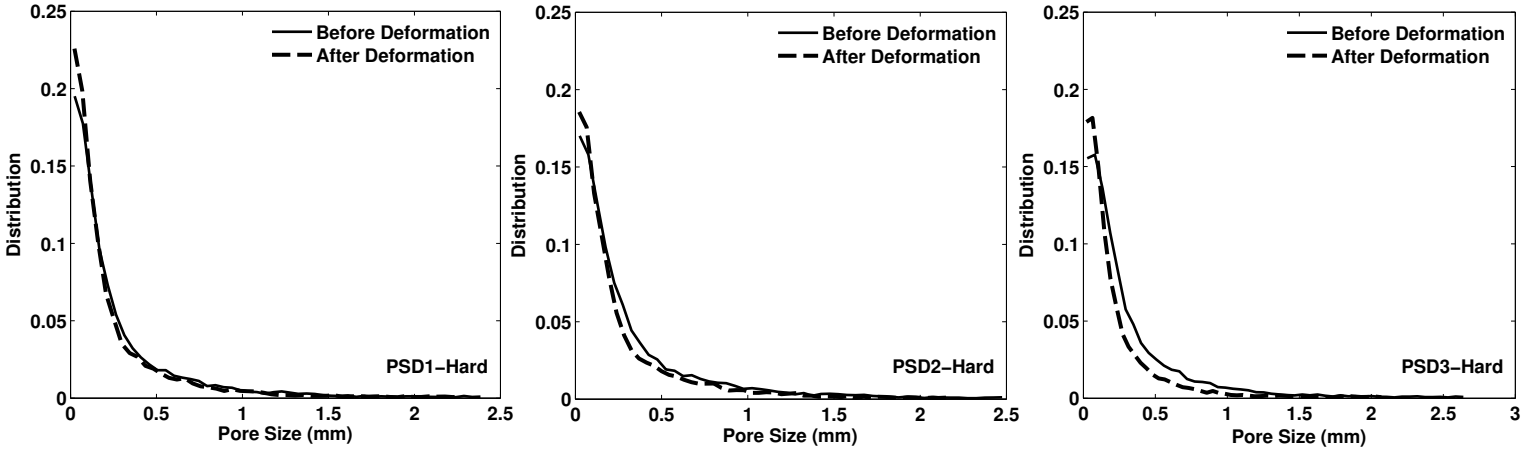

Figure 3: The computed pore-size distributions of the dense packings of hard particles with the three particle-size distributions shown in Fig. 2.

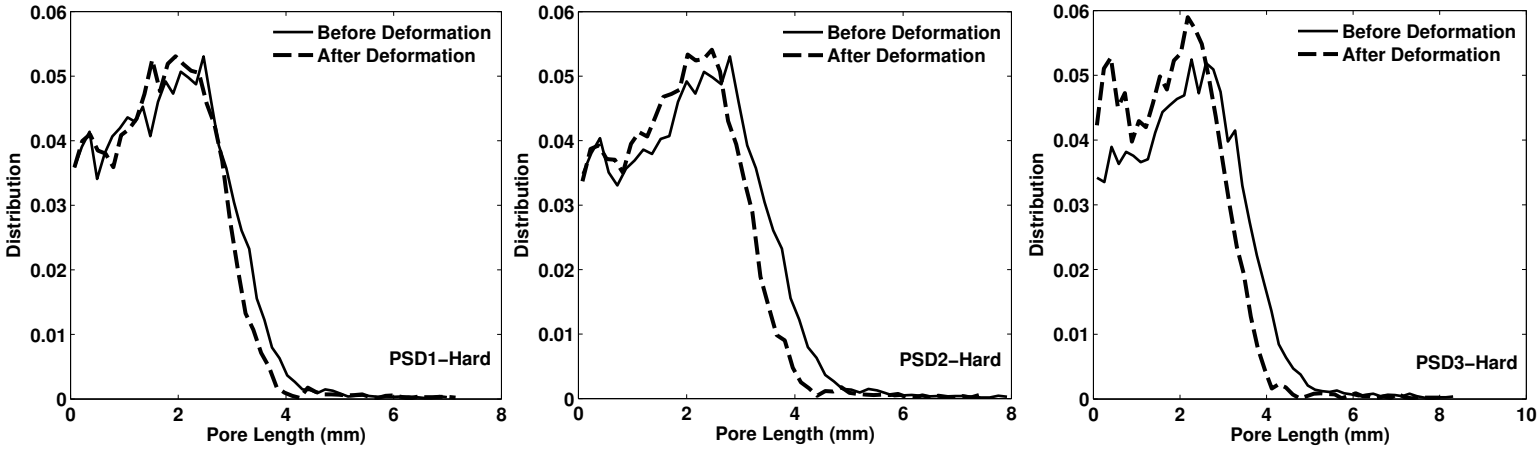

Figure 4: The computed pore-length distributions of the dense packings of hard particles with the three particle-size distributions shown in Fig. 2.

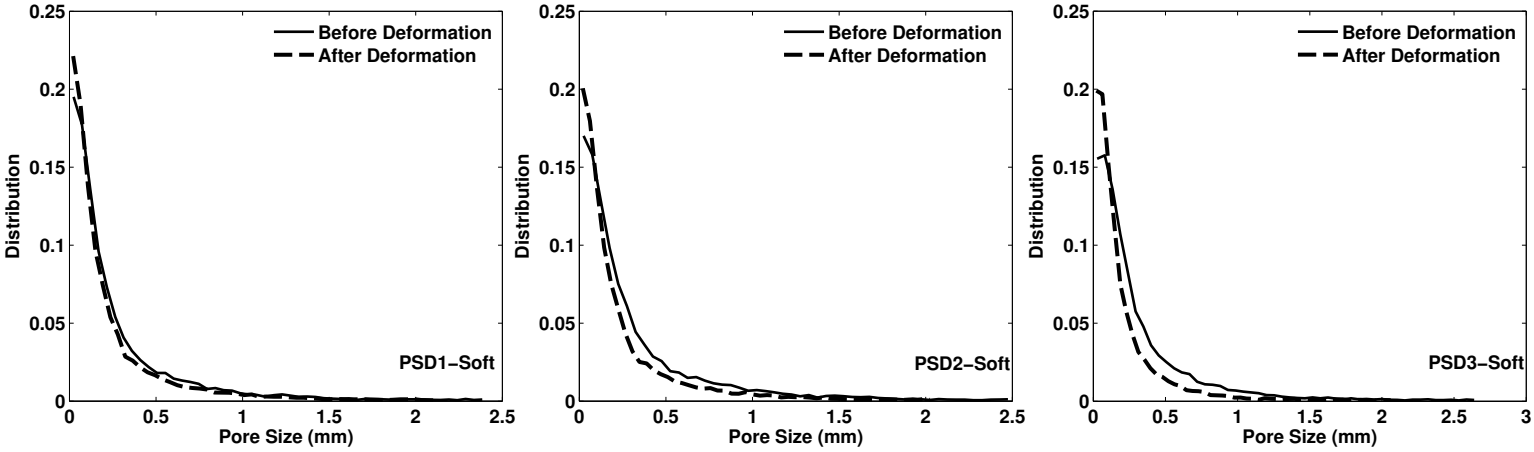

Figure 5: The computed pore-size distributions for the dense packings of soft particles and the three particle-size distributions shown in Fig. 2.

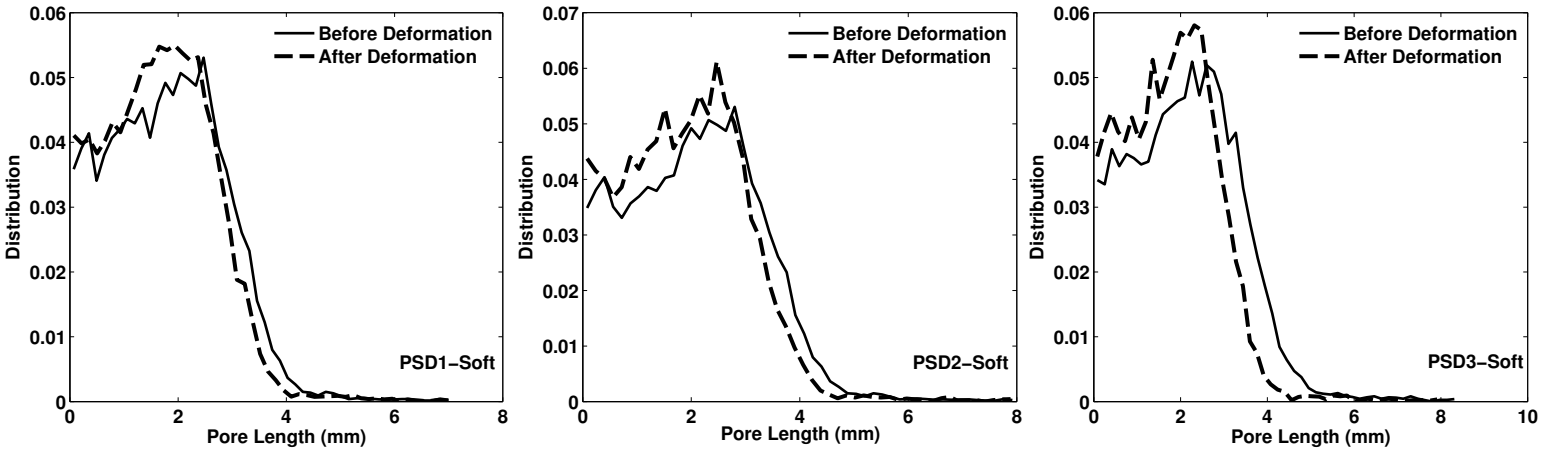

Figure 6: The computed pore-length distributions for the dense packings of soft particles and the three particle-size distributions shown in Fig. 2.

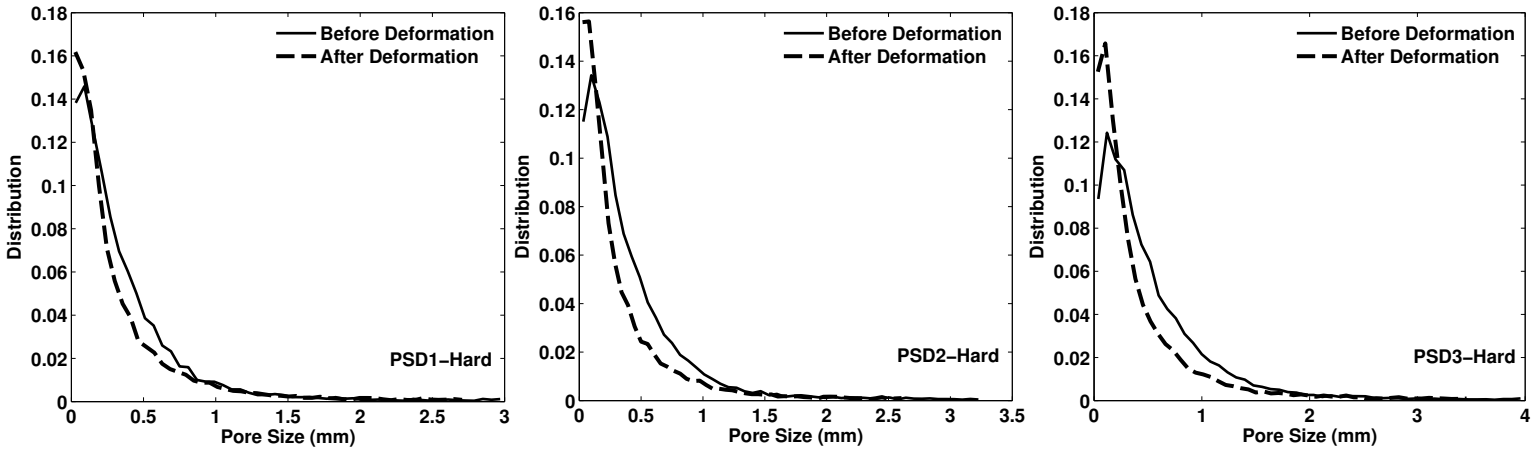

Figure 7: The computed pore-size distributions of random packings of hard particles with an initial porosity 0.54 and the three particle-size distributions shown in Fig. 2.

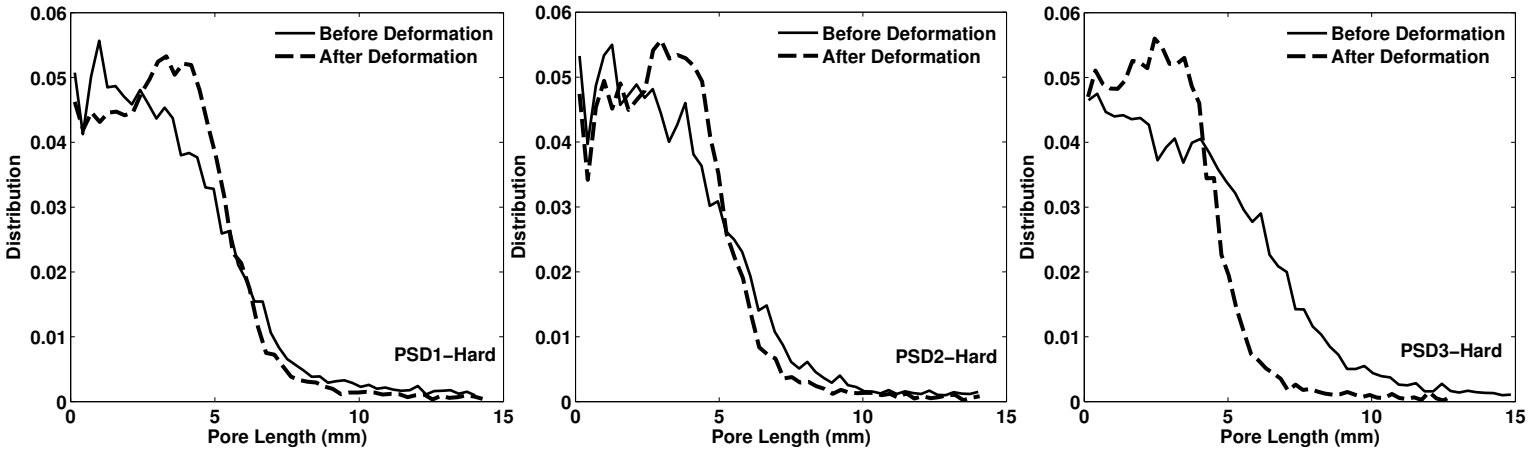

Figure 8: The computed pore-length distributions of the random packings of hard particles with an initial porosity 0.54 and the three particle-size distributions shown in Fig. 2.

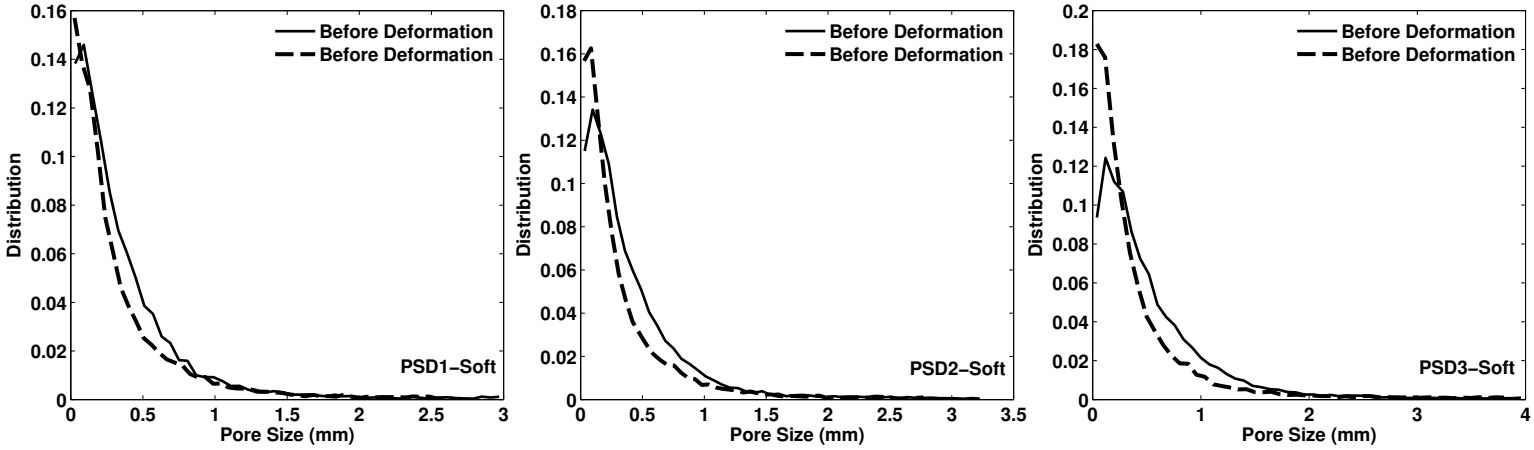

Figure 9: Same as in Fig. 7, but for random packings of soft particles.

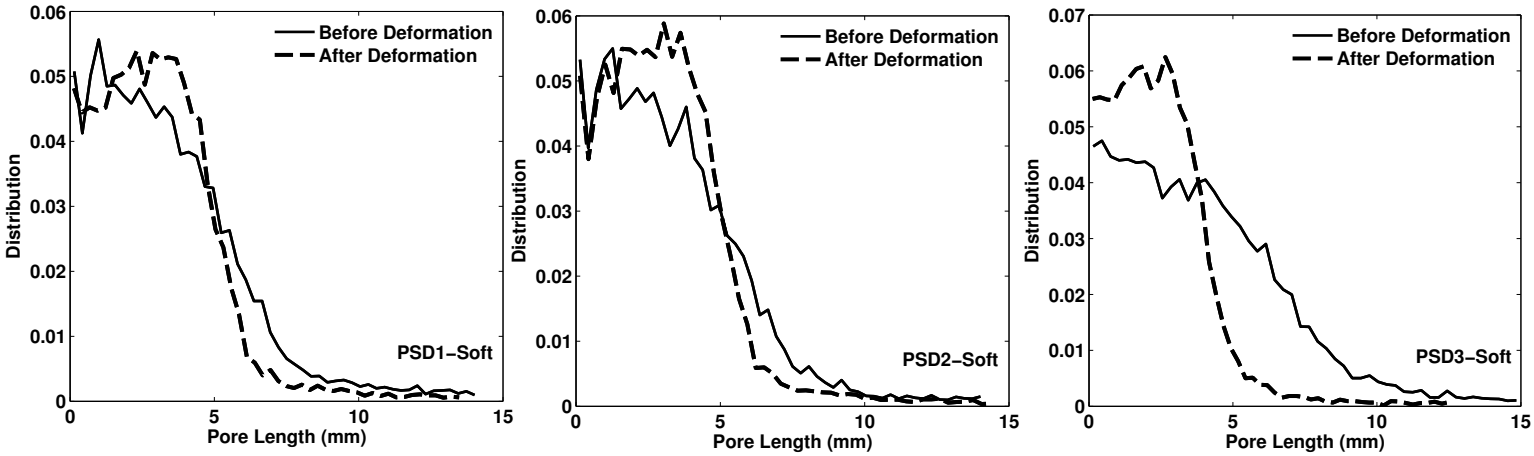

Figure 10: Same as in Fig. 8, but for random packings of soft particles.

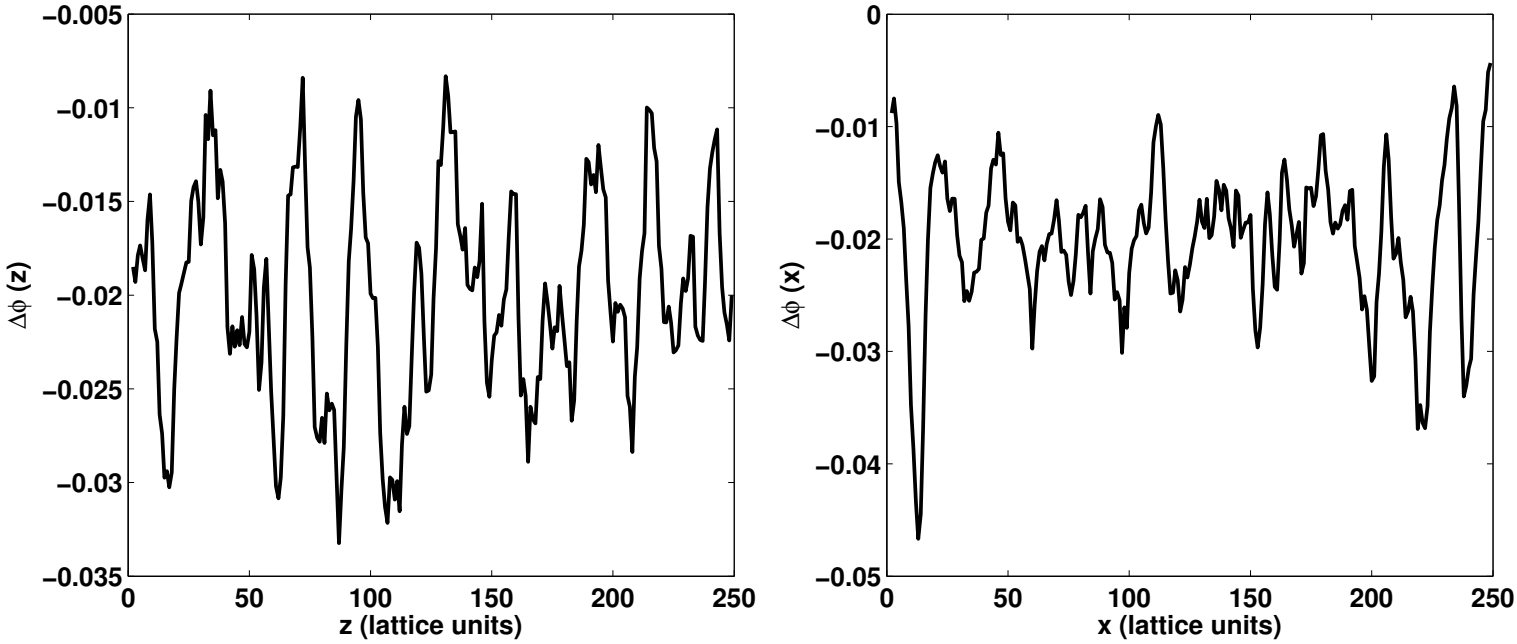

Figure 11: Fluctuations $\Delta\phi$ in the porosity in the strain (z) and flow (x) directions.

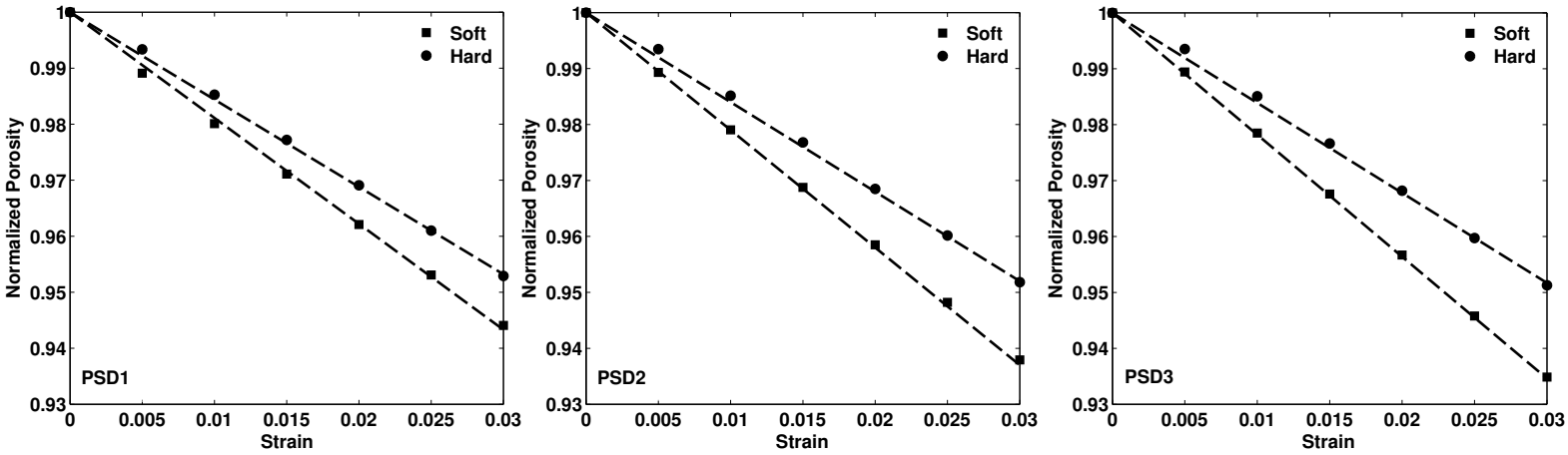

Figure 12: Dependence of porosity of the dense packings on the external strain. The particle-size distributions are shown in Fig. 2, and the porosities have been normalized by their initial values before deformation.

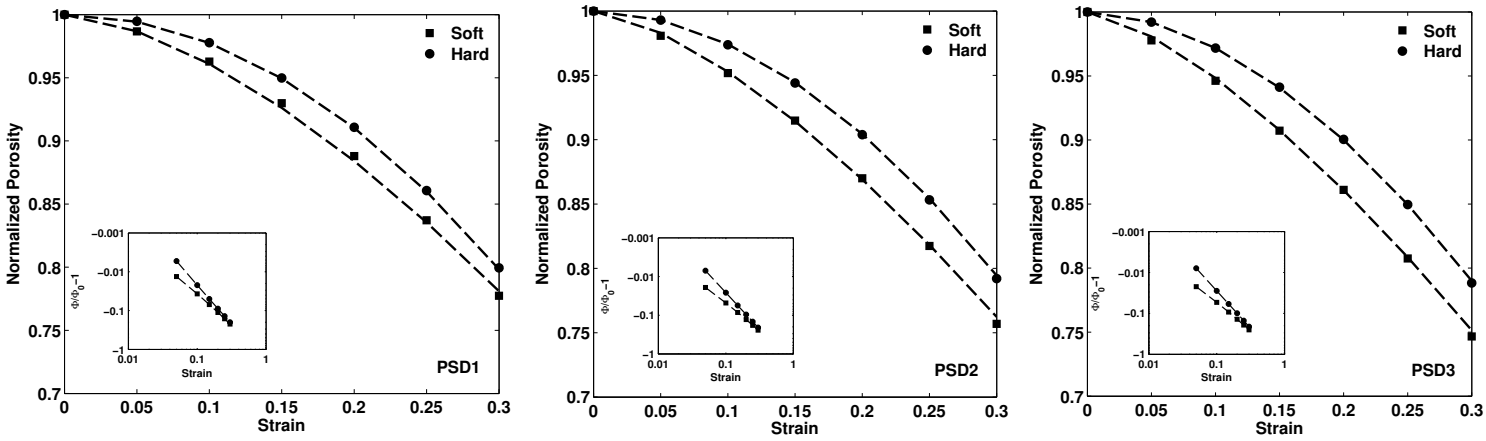

Figure 13: Same as in Fig. 12, but for loose packing with an initial porosity of 0.54. The insets show the logarithmic plots of the same.

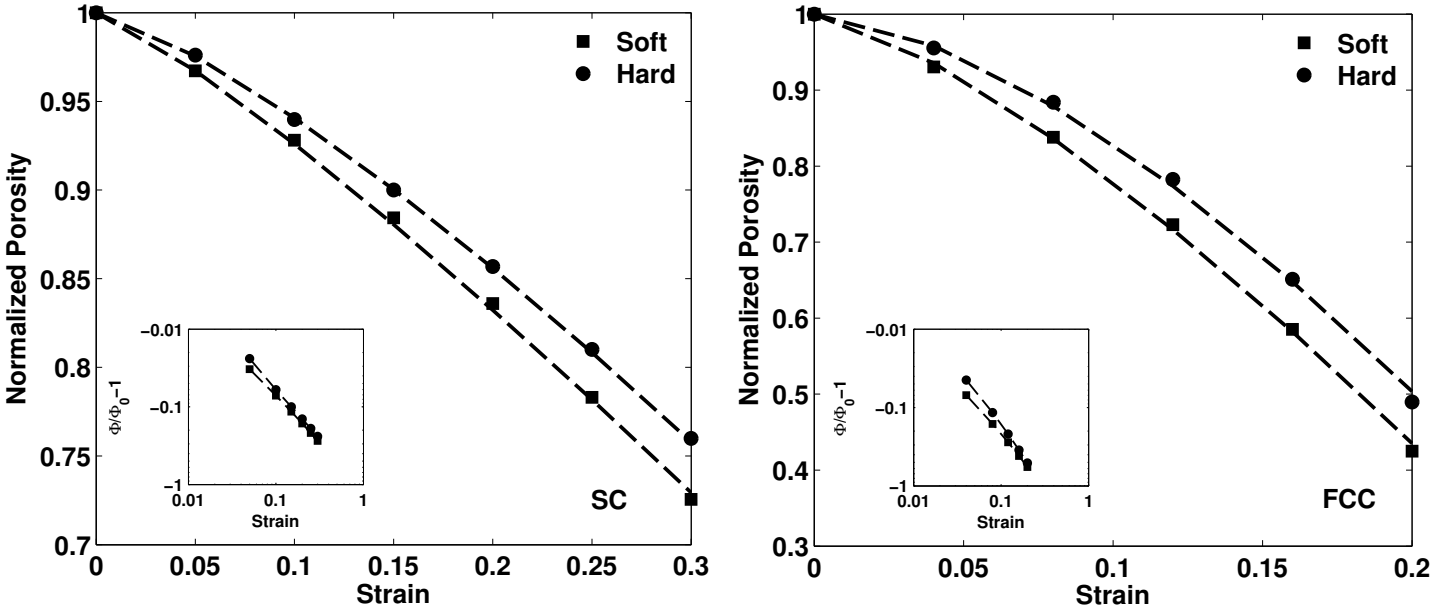

Figure 14: Same as in Fig. 12, but for the regular packings. The insets show the logarithmic plots of the same.

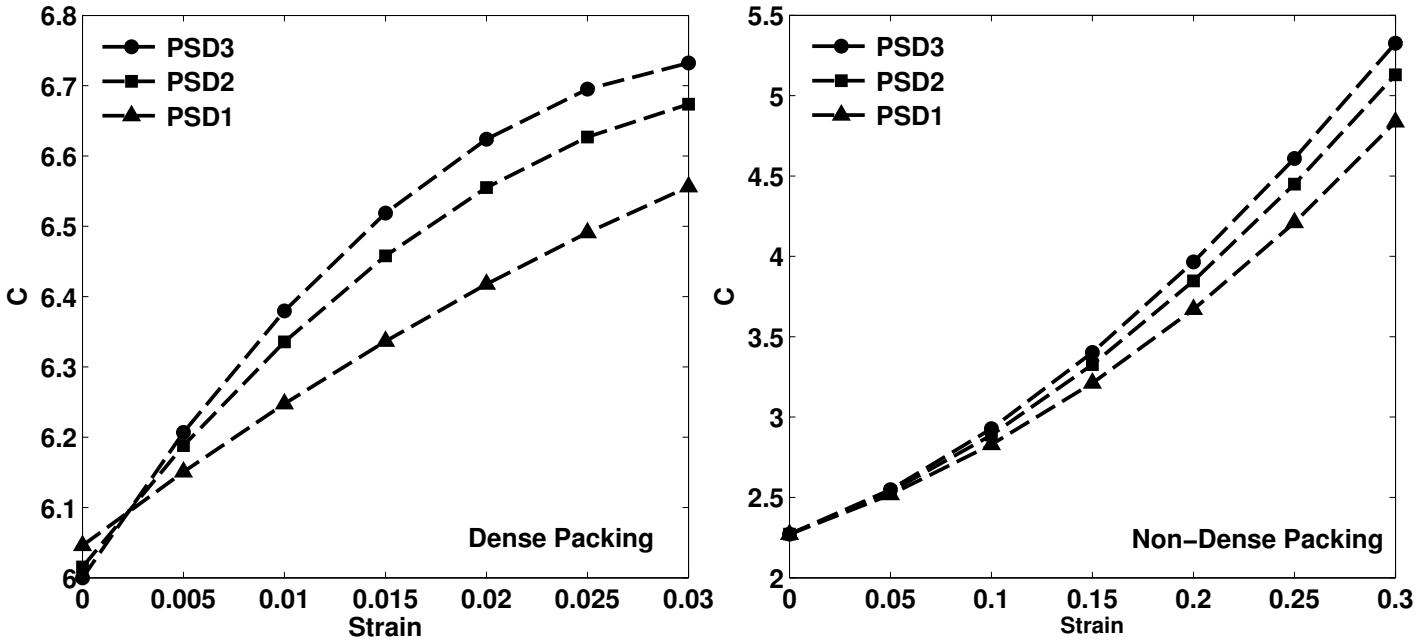

Figure 15: Dependence of the average number of contacts C on the external strain in random packings of soft particles and the particle-size distributions shown in Fig. 2.

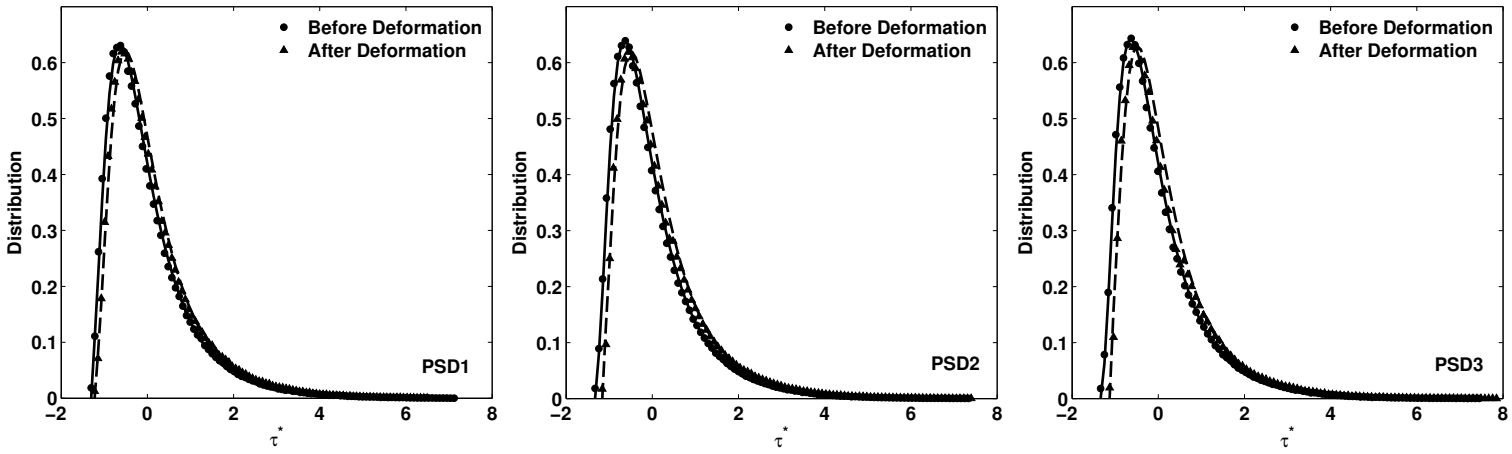

Figure 16: The distributions of the computed normalized stresses, exerted by the fluid in the pore space of the dense random packings of soft particles. The curves represent fit of the numerical data to the log-normal distribution, Eq. (23).

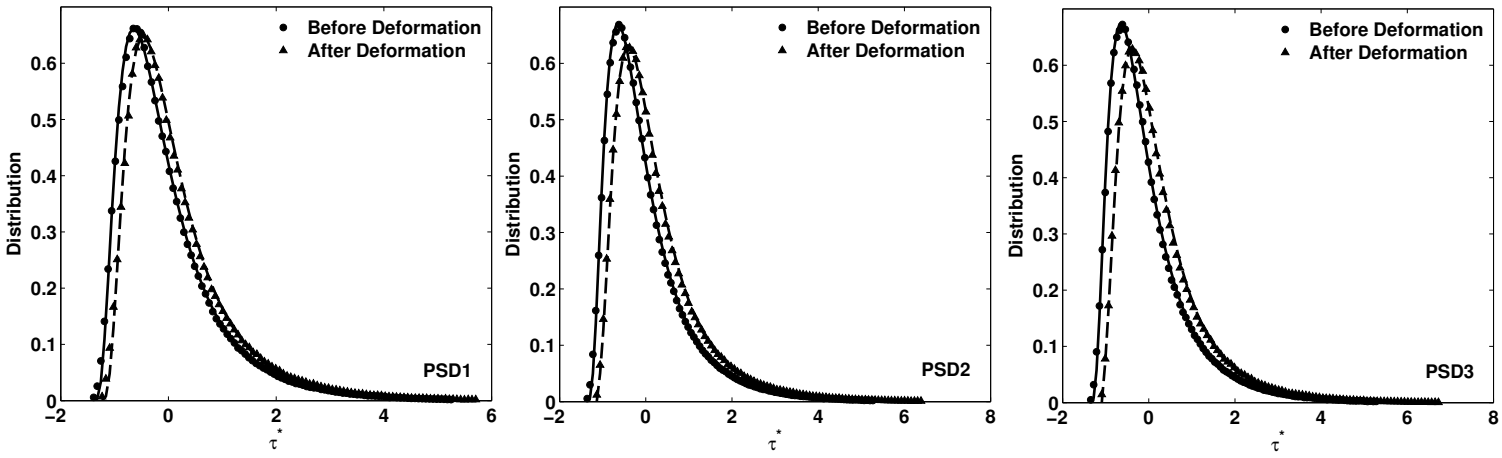

Figure 17: The distribution of the computed normalized stresses, exerted by the fluid in the pore space of a loose packing of soft particles with an initial porosity of 0.54. The curve show the fit of the numerical data to Eq. (23).

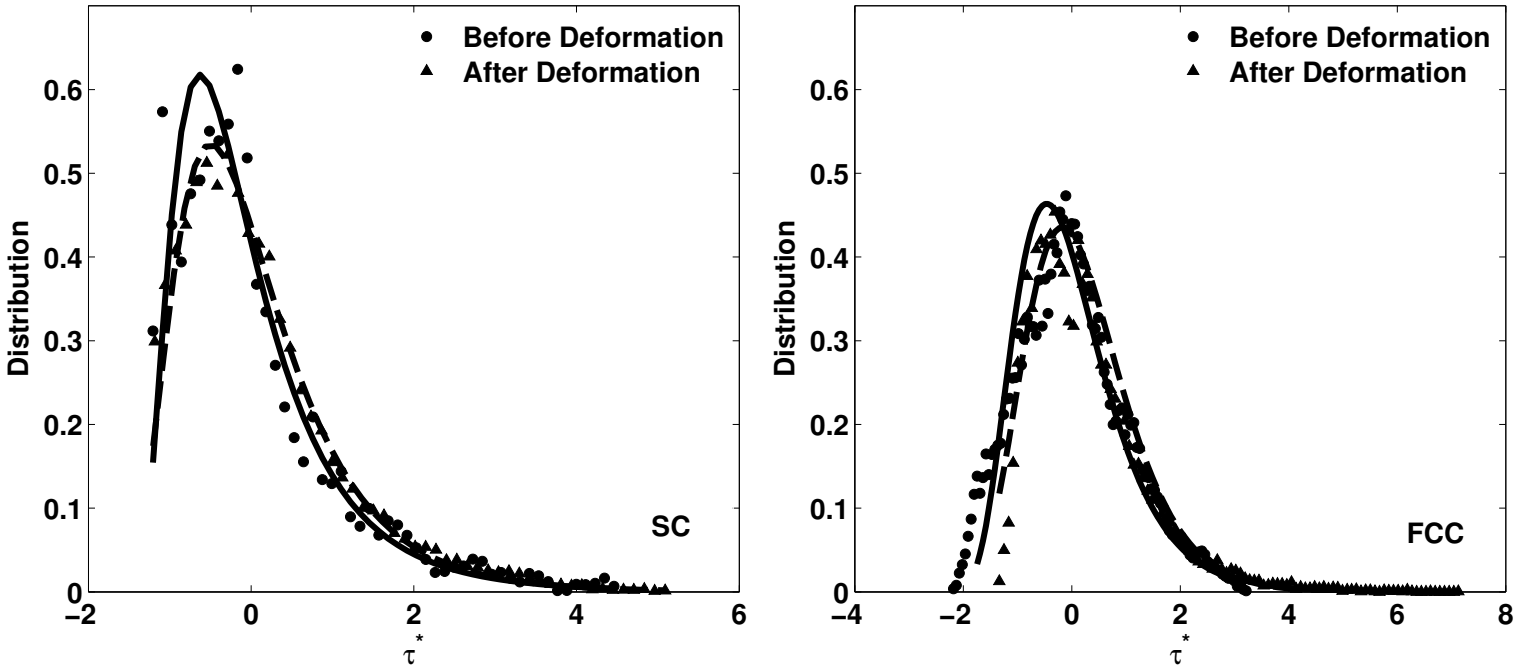

Figure 18: The distribution of the computed normalized stresses, exerted by the fluid in the pore space of regular packings of soft equal-size particles. (a) Simple-cubic (SC) packing at an external strain of 0.2, and (b) face-centered cubic (FCC) packing at an external strain of 0.2.

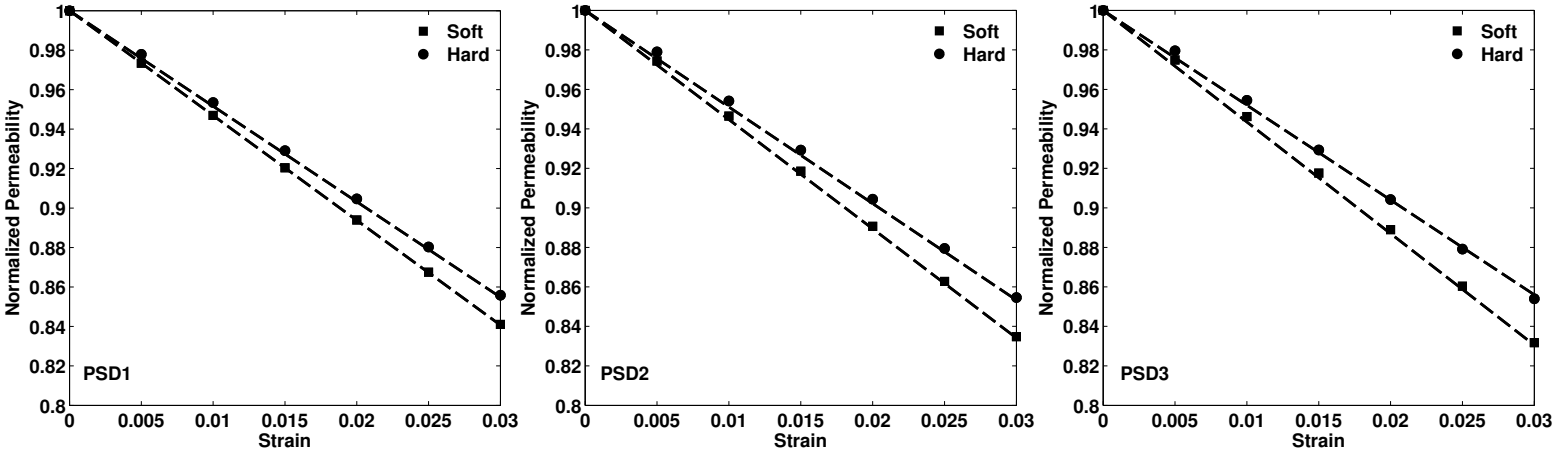

Figure 19: Dependence of the permeability of dense random packings on the external strain. The particle-size distributions are those shown in Fig. 2. The permeabilities are normalized by their values before deformation.

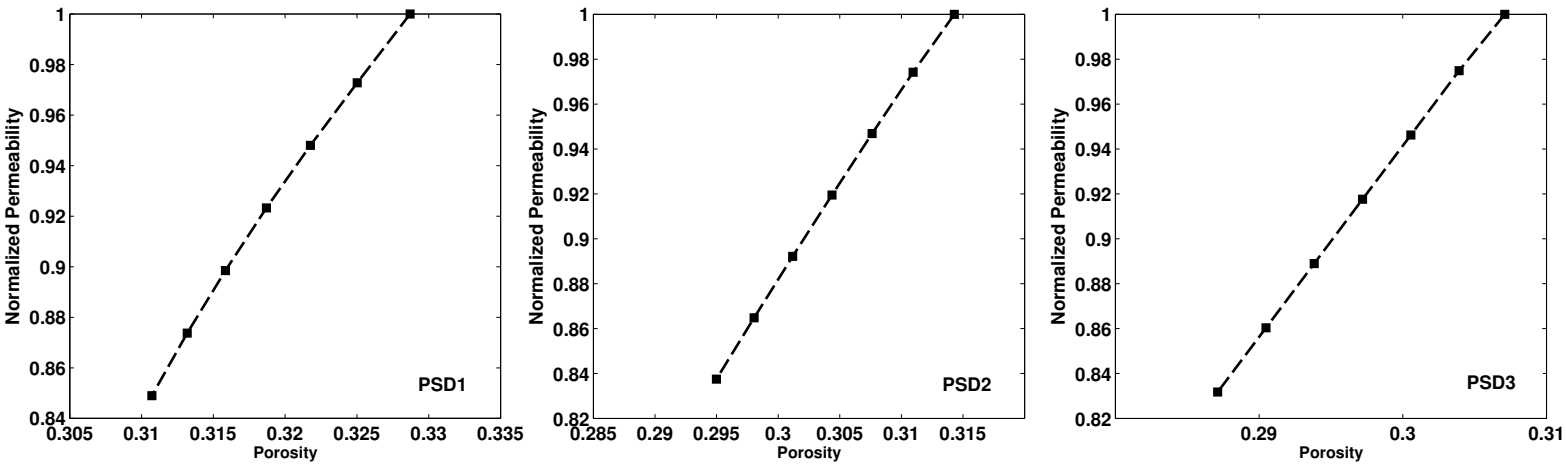

Figure 20: Dependence of the permeability of dense random packings on the porosity. The particle-size distributions are those shown in Fig. 2. The permeabilities are normalized by their values before deformation.

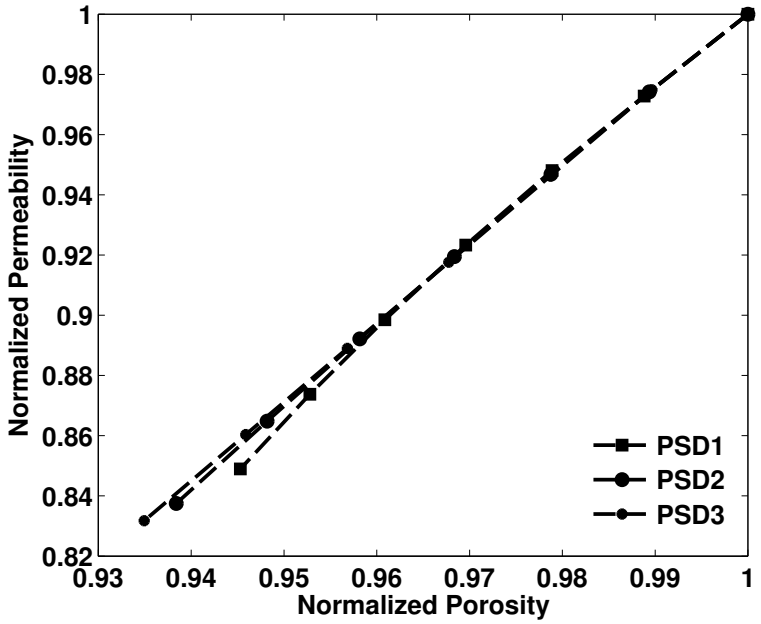

Figure 21: Collapse of the permeability-porosity data of Fig. 20 onto a universal curve.

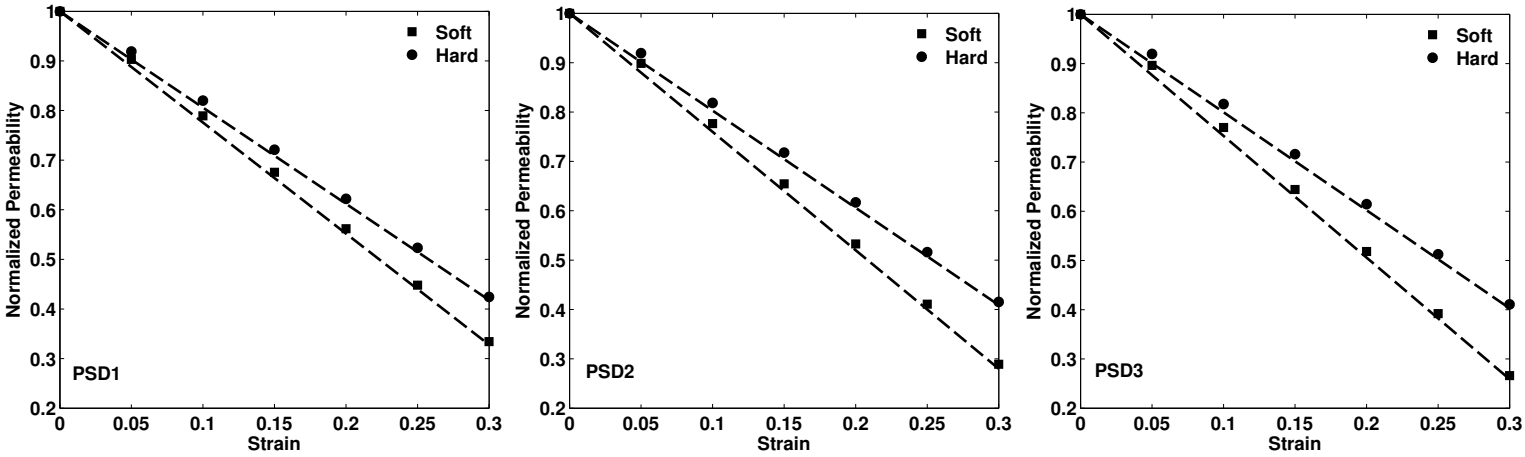

Figure 22: Same as in Fig. 19, but for random loose packings with an initial porosity of 0.54.

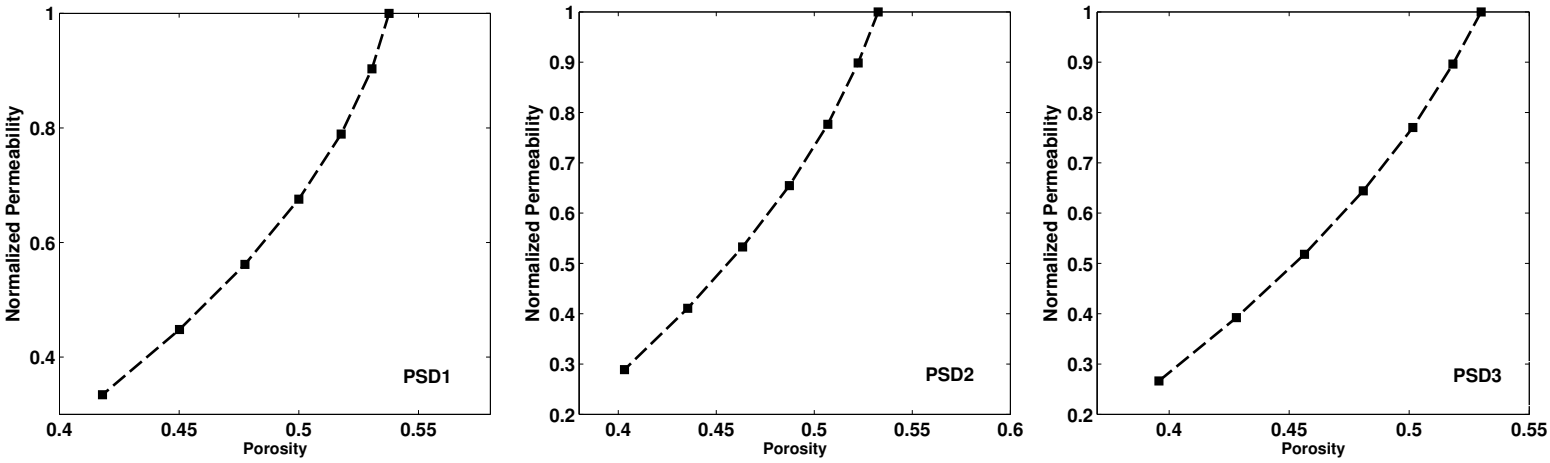

Figure 23: Dependence of the permeability of the random loose packings on the porosity. The initial porosity was 0.54. The particle-size distributions are those shown in Fig. 2. The permeabilities are normalized by their values before deformation.

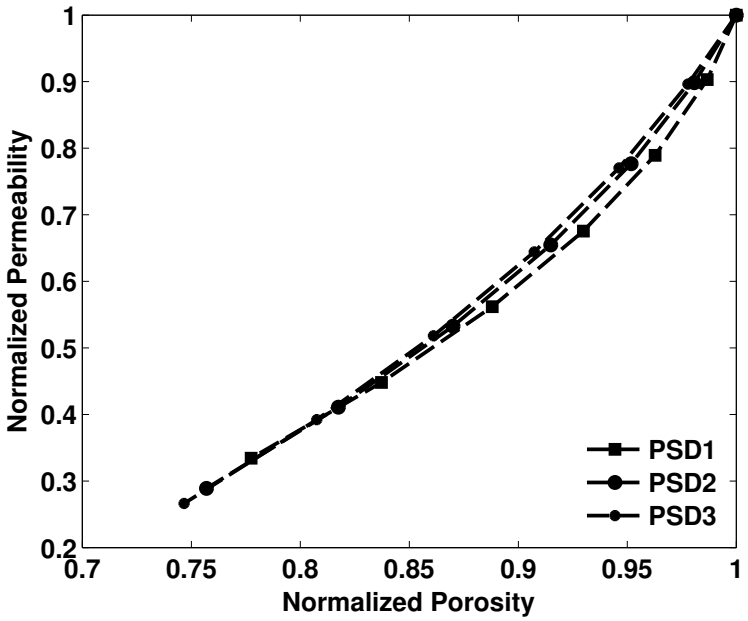

Figure 24: Collapse of the permeability-porosity data of Fig. 23 onto a universal curve.

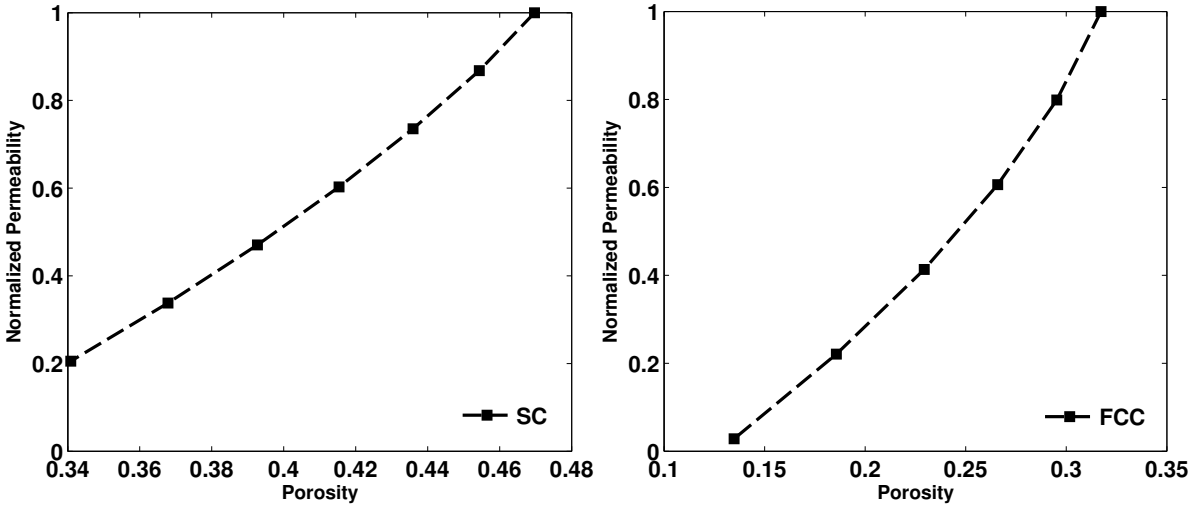

Figure 25: Dependence on the external strain of the permeability of the simple-cubic (SC) and face-centered cubic (FCC) packings of particles. The permeabilities are normalized by their values before deformation.

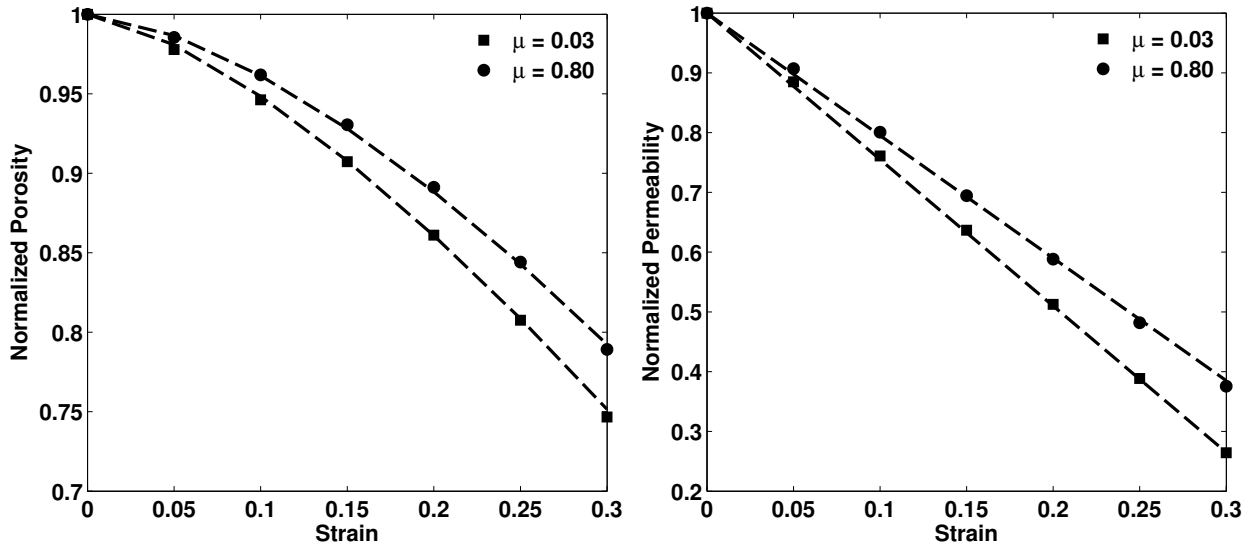

Figure 26: Dependence on the friction coefficient μ of the permeability and porosity of a random packing of soft particles with an initial porosity of 0.54. The particle-size distribution is PSD3, shown in Fig. 2.